3

Exchange Flow through the Strait of Gibraltar as Simulated by a σ-Coordinate Hydrostatic Model and a z-Coordinate Nonhydrostatic Model

Gianmaria Sannino[1], J. C. Sánchez Garrido[2], L. Liberti[3], and L. Pratt[4]

3.1. INTRODUCTION

The Mediterranean Sea is a semi-enclosed basin displaying an active thermohaline circulation (MTHC) that is sustained by the atmospheric forcing and controlled by the narrow and shallow Strait of Gibraltar (hereinafter SoG). The atmospheric forcing drives the Mediterranean basin toward a negative budget of water and heat. Over the basin, evaporation exceeds the sum of precipitation and river discharge, while a net heat flux is transferred to the overlying atmosphere through the sea surface. These fluxes are balanced by the exchange flow that takes place in Gibraltar. Within the SoG, the MTHC takes the form of a two-way exchange: an upper layer of fresh and relatively warm Atlantic water spreads in the Mediterranean basin, and a lower layer of colder and saltier Mediterranean water sinks as a tongue in the North Atlantic at intermediate depths. The interaction between the intense tidal forcing [*Candela et al.*, 1990] and the complex geometry of the SoG (Figure 3.1a) influences the two-way exchange via hydraulic control [*Bryden and Stommel*, 1984]. The exchange is subject to vigorous mixing and entrainment [*Wesson and Gregg*, 1994] as well as intermittent hydraulic controls over the main sills and in its narrowest sections [*Sannino et al.*, 2007; *Sannino et al.*, 2009a]. The simultaneous presence in the SoG of at least two cross sections in which the exchange is controlled drives the strait dynamics toward the so-called maximal regime [*Bryden and Stommel*, 1984; *Armi and Farmer*, 1988]. If the exchange is subject to only one hydraulic control, the regime is called submaximal. The two regimes have different implications for property fluxes, response time, and other physical characteristics of the coupled circulation in the SoG and Mediterranean Sea. The maximal regime can be expected to have larger heat, salt, and mass fluxes and to respond more slowly to changes in stratification and thermohaline forcing within the Mediterranean Sea and the North Atlantic Ocean [*Sannino et al.*, 2009a].

As first recognized by *Bray et al.* [1995], the strong entrainment and mixing present in the Strait of Gibraltar lead to the formation of a thick interfacial layer where density and velocity change gradually in the vertical direction. They also argued that the classical two-layer approach used to describe the two-way exchange was insufficient to account for the flow regime in the SoG. They found that a three-layer system, which includes an active interface layer, best represents the exchange through the SoG. The presence of a thick interfacial layer complicates the estimation of the hydraulic state of the flow exchange using the two-layer hydraulic theory. Such difficulty has been recently overcome by *Sannino et al.* [2007] who analyzed for the fist time the hydraulic regime of the exchange flow applying a three-layer hydraulic theory. Doing so they considered the thick interfacial layer as an active participant of the hydraulic regime. The hydraulic studies conducted by *Sannino et al.* [2007] were based on the analysis of numerical simulations. The simulations were carried out using a σ-coordinate model

[1] *Climate and Impact Modeling Lab—Energy and Environment Modeling Unit—ENEA, CR Casaccia, Rome, Italy*

[2] *Grupo de Oceanografía Física. Dpto. Física Aplicada II, Campus de Teatinos, University of Malaga, Malaga, Spain*

[3] *Istituo Superiore per la Protezione e la Ricerca Ambientale, Rome, Italy*

[4] *Woods Hole Oceanographic Institution, Woods Hole, Massachusetts, USA*

The Mediterranean Sea: Temporal Variability and Spatial Patterns, Geophysical Monograph 202. First Edition.
Edited by Gian Luca Eusebi Borzelli, Miroslav Gačić, Piero Lionello, and Paola Malanotte-Rizzoli.

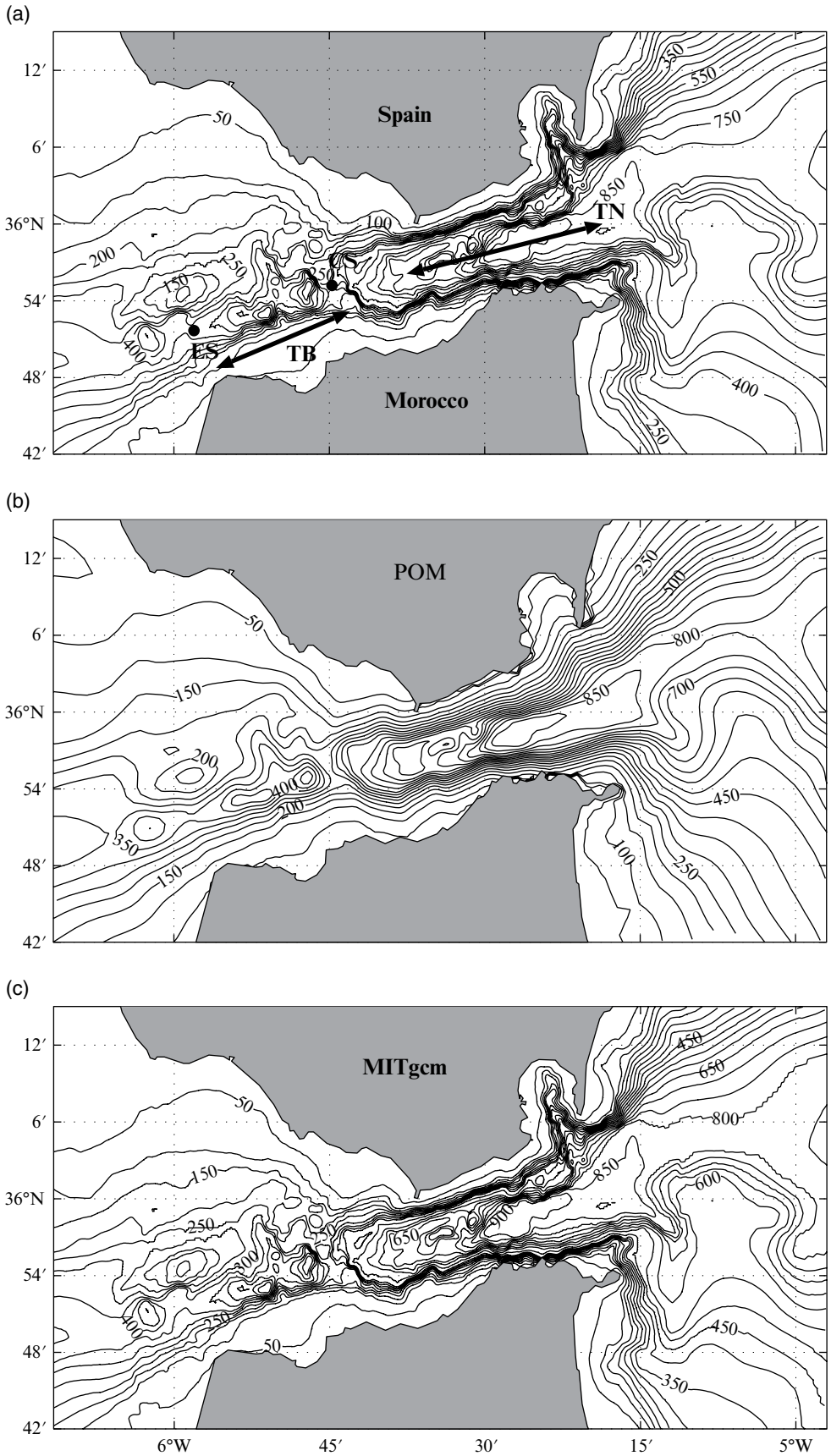

Figure 3.1 (a) Original bathymetric chart of the Strait of Gibraltar; (b) Bathymetry as represented in the σ-coordinate POM; (c) Bathymetry as represented in the z-level, partial cells MITgcm.

essentially based on the Princeton Ocean Model [POM; *Blumberg and Mellor*, 1987].

In the last 15 years, many models of different complexity have been implemented to study most of the aspects of the flow exchange through the SoG. However, the only three-dimensional model able to reproduce most of the features of the exchange flow was the one initially implemented by *Sannino et al*. [2007] and subsequently improved by *Sannino et al*., [2009a]. The earliest version of the model was developed by *Sannino et al*. [2002] to study the mean flow exchange; subsequently the model was improved by *Sannino et al*. [2004] who introduced the tidal forcing. Recently, the model has been used to test the applicability of classical two-layer, one-dimensional hydraulic theory to the SoG [*Sannino et al*., 2007, 2009a]. The model has been also used to estimate the Mediterranean water outflow at the western end of the SoG in a combined observational-modeling work [*Sanchez-Roman et al*., 2009], and to assess kinematic properties of internal waves in the area [*Garrido et al*., 2008]. The extensive use of POM in the study of different aspects of the flow exchange has led to an almost complete validation of the model. Results have been validated against most of the available *in situ* data.

According to the validation analysis so far performed, it appears that POM is able to capture, in a reasonable way, most of the main features of the exchange flow. However, there are some aspects of the strait hydrodynamics that could not be well reproduced by the model. This especially concerns the evolution of the internal tidal bore generated in the main sill area. After its generation, the bore progresses toward the Mediterranean, evolving into a series of short internal solitary waves of large amplitude [*Vlasenko et al*., 2009]. These waves are strongly nonlinear and nonhydrostatic, thus their modeling requires fully nonhydrostatic codes such as, for example, MITgcm [*Marshall et al*., 1997a] or SUNTANS [*Fringer et al*., 2006].

Although the poor representation of the bore generation and propagation was an expected outcome for POM, there still remain some open questions regarding the effects produced by the hydrostatic assumption, the vertical and horizontal resolution adopted, and the parameterization used for mixing on the simulated hydraulic regime. Thus, the main goal of this study is the investigation of the effects produced by these factors on the simulated hydraulic behavior of the SoG by the nonhydrostatic assumption, the resolution adopted, and the parameterization used. To this purpose the exchange flow simulated by POM has been compared with the exchange flow simulated by a very high-resolution, fully nonhydrostatic model implemented for the strait region. The nonhydrostatic model is based on the z-coordinate MITgcm code (http://mitgcm.org). As pointed out by *Legg et al*. [2006], the nonhydrostatic version of the MITgcm, when implemented at very high resolution, is able to capture the largest-scale mixing processes responsible for entrainment. Thus, the model does not need specific parameterizations for the entrainment. The evaluation of the impact of these novel features on the water exchange and hydraulics regime of the SoG is one of the scopes of this paper. As will be demonstrated in the following, these particular features allow the simulation performed with MITgcm to be used as a benchmark against which the POM simulation and, more in general, any numerical model simulating the dynamics of the SoG at lower resolution can be compared. Thus, the overall objective of the present study is a systematic comparison of the main features simulated by POM, as for example the three-layer structure, the transports, and the hydraulic regime simulated, with those obtained by MITgcm.

The remainder of the paper is organized as follows: the two models are described in section 2 and validated in section 3; the comparison of the models in terms of the simulated internal wave field, three-layer properties, and hydraulics is shown in section 4; while conclusions will be discussed in section 5.

3.2. MODELS DESCRIPTION AND INITIALIZATION

The two models used in this work are the σ-coordinate Princeton Ocean Model [POM; *Blumberg and Mellor*, 1987] as implemented by *Sannino et al*. [2009a], and the height vertical coordinate Massachusetts Institute of Technology general circulation model [MITgcm; see *Marshall et al*., 1997a, b, as implemented by *Garrido et al*., 2012].

3.2.1. POM

The hydrostatic POM model as been implemented by *Sannino et al*. [2002] and *Sannino et al*. [2009a] to investigate different aspects of the circulation that take place in the SoG: mean and tidal exchange [*Sannino et al*., 2002; *Sannino et al*., 2004], time and spatial variability of the internal bore propagation [Garrido et al., 2008], estimation of the Mediterranean water outflow [*Sanchez-Roman et al*., 2009], and hydraulic regimes [*Sannino et al*., 2007; *Sannino et al*., 2009a].

An extensive description of the model setting can be found in *Sannino et al*. [2004, 2009a]; some aspects relevant for the comparison with MITgcm are described in the following. The POM version used in *Sannino et al*. [2009a], is the one generally known as *pom*98 with the only exception for the advection scheme. As default POM uses a second-order centered (both spatially and temporally) scheme. It is well known that such a scheme is dispersive. Dispersion is more evident in presence of strong

density gradients where it creates spurious temperature and salinity values (over- and undershooting problems). Thus, the presence of density gradients within the Strait of Gibraltar makes the centered scheme unable to simulate the water exchange. To overcome this problem, the second-order, sign-preserving Multidimensional Positive Definite Advection Transport Algorithm (MPDATA), as developed by *Smolarkiewicz* [1984] and implemented by *Sannino et al*. [2002], has been used. MPDATA is a flux corrected upstream scheme, that is, an upstream scheme characterized by a reduced implicit diffusion. The numerical diffusion is reduced through an iterative method based on antidiffusive velocities, which is applied to correct the excessive numerical diffusion of standard upstream scheme. The repeated procedure yields a positive definite advection algorithm with second-order accuracy. The number of iterations is optional; each additional iteration increases the solution accuracy and the computation time: the number of iterations chosen in *Sannino et al*. [2009a] was three.

The vertical mixing coefficients were obtained from the Mellor-Yamada turbulence scheme [*Mellor and Yamada*, 1982]. As demonstrated by *Ezer* [2005], the Mellor-Yamada scheme is able to explicitly capture the mixing processes responsible for entrainment, so there is no need for specific parameterizations of entrainment in POM. The horizontal momentum, heat, and salt small-scale mixing processes are parameterized via the Laplacian, along-sigma, velocity, and grid space dependent Smagorinsky diffusion scheme [*Smagorinsky*, 1963]. Normal velocities are set to zero along coastal boundaries. At the bottom, adiabatic boundary conditions are applied to temperature and salinity and a quadratic bottom friction, with a prescribed drag coefficient, is applied to the momentum flux. This is calculated by combining the velocity profile with the logarithmic law of the wall:

$$C_D = \max\left[2.5\times10^{-3}, k^2 \ln\left(\Delta z_b / z_0\right)\right] \qquad (1)$$

where k is the Von Karman constant, z_0 is the roughness length set to 1 cm, and Δz_b is the distance from the bottom of the deepest velocity grid point.

The model grid extends longitudinally from the Gulf of Cadiz to the Alboran Sea. The grid has a nonuniform horizontal spacing (see Figure 6 of *Sannino et al*. [2009a]); the resolution is finer in the strait, where Δx (Δy) is 593 m (485 m) around Camarinal Sill (CS) (Figure 3.2a), while Δx (Δy) is 10 Km (20 Km) and 8 Km (15 Km) at the eastern and western ends, respectively. The vertical grid has 32 σ levels, logarithmically distributed at the surface and at the bottom, and uniformly distributed in the rest of the water column. In a water depth of 1000 m, the upper and lower six σ levels are concentrated in about 100 m, while the remaining levels are equally spaced (40 m). Model bathymetry has been obtained through a bilinear interpolation of data obtained merging the ETOPO2 bathymetry [*NOAA*, 2001] with the very high-resolution bathymetry chart of *Sanz et al*. [1992]. Moreover, to reduce the well-known pressure gradient error produced by σ coordinates in regions of steep topography [*Haney*, 1991], an additional smoothing was applied in order to reach values of $\delta H/H < 0.2$, where H is the model depth as suggested by *Mellor et al*. [1994]. The resulting model topography (Figure 3.1b**)** is different from the original one especially in the coastal regions where the continental slope has been significantly broadened. Two open boundaries are defined at the eastern and western ends of the computational domain. Here an Orlanski radiation condition [*Mellor et al*., 1994] is used for the depth-dependent velocity, while a forced-Orlanski radiation condition [*Bills and Noye*, 1987] is used for the surface elevation and a zero gradient condition for the depth-integrated velocity. Boundary conditions for both temperature and salinity are specified using an upwind advection scheme that allows the advection of temperature and salinity into the model domain under inflow conditions.

The model starts from rest and is forced at the open boundaries through the specification of the surface tidal elevation that is characterized by the principal two semidiurnal and two diurnal harmonics: M_2, S_2, O_1, K_1. Amplitude and phase of these harmonics have been computed via the OTIS package [*Egbert and Erofeeva*, 2002]. Finally, the initial conditions for salinity and temperature have been taken from the climatologic Medar-MedAtlas Database [*MEDAR Group*, 2002] for the month of April.

The model was initially run without tidal forcing in order to achieve a steady two-way exchange system. Then the model was forced by tidal components in order to achieve a stable time-periodic solution. After this spin-up phase, the model was run for a further tropical month (27.321 days) that represents our reference experiment (Exp-POM). The term *time-averaged* that will be used in the remaining part of the paper refers to the average over this tropical month period.

3.2.2. MITgcm

MITgcm is the other model used in this work. MITgcm solves the fully nonlinear, nonhydrostatic Navier–Stokes equations under the Boussinesq approximation for an incompressible fluid with a spatial finite-volume discretization on a curvilinear computational grid. The model formulation includes implicit nonlinear free surface [*Campin et al*., 2004], rescaled vertical height (z^*) coordinates [*Adcroft et al*., 2004], and two-way nesting capabilities [*Sannino et al*., 2009b]. An extensive online documentation is at http://mitgcm.org.

The model domain extends from 6.3°W to 4.78°W and is discretized by a nonuniform curvilinear orthogonal

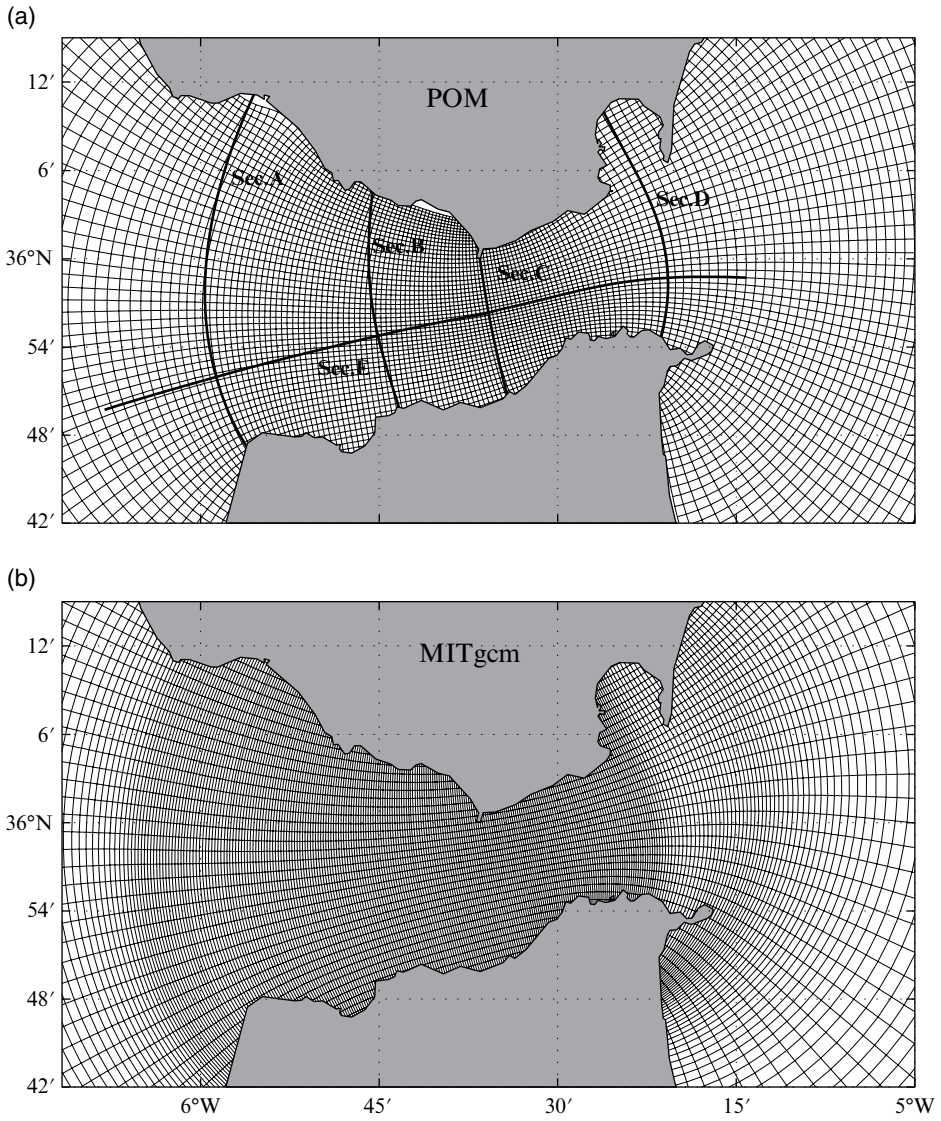

Figure 3.2 (a) Horizontal grid used in POM. Black lines indicate cross-sections referred in the text; (b) Horizontal grid used in the MITgcm (note that only 25% of the actual grid lines are shown).

grid of 1440 x 210 points (Figure 3.2b). Spatial resolution along the axis of the strait, Δx (across the strait axis, Δy), ranges between 46 and 63 m (175 and 220 m) in the area of CS. The mesh size is always less than 70 m (340 m) in the middle of the strait between Espartel Sill and CS, and less than 70 m (200 m) between CS and Tarifa Narrow. The vertical grid has 53 z-levels spaced 7.5 m in the upper 300 m, and their thickness gradually increases to a maximum of 105 m for the remaining 13 bottom levels.

The model topography (Figure 3.1c) has been obtained through a bilinear interpolation of the same initial data described in the POM section, however, in this case, no additional smoothing has been applied. The very high horizontal resolution adopted in MITgcm, together with the partial cell formulation, result in a very detailed description of the bathymetry. The only appreciable differences with respect to the original bathymetric data are confined on the eastern and western ends of the model in the region where the depth is greater than 800 m. No-slip conditions were imposed at the bottom and lateral solid boundaries. The selected tracer advection scheme is a third-order direct space-time flux limited scheme due to *Hundsdorfer et al.* [1995]. Following the numerical experiments conducted by *Vlasenko et al.* [2009] to investigate the 3-D evolution of LAIWs in the Strait of Gibraltar, the turbulent closure parametrization for vertical viscosity and diffusivity proposed by *Pacanowski and Philander* [1981] was used. Their Richardson-number-dependent expression reads:

$$\nu = \frac{\nu_0}{(1+\alpha \mathrm{Ri})^n} + \nu_b, \quad \kappa = \frac{\nu}{(1+\alpha \mathrm{Ri})} + \kappa_b, \qquad (2)$$

where $\mathrm{Ri} = N^2(z)/\left(u_z^2 + v_z^2\right)$ is the Richardson number, $\nu_b = 1.5 \cdot 10^{-4}$ m^2 s^{-1}, $\kappa_b = 1 \cdot 10^{-7}$ m^2 s^{-1} are background values, and $\nu_0 = 1.5 \cdot 10^{-2}$ m^2 s^{-1}, $\alpha = 5$ and $n = 1$ are adjustable parameters. Horizontal diffusivity coefficient is $\kappa_h = 1 \cdot 10^{-2}$ m^2 s^{-1}, whereas variable horizontal viscosity follows the parameterization of *Leith* [1968].

Initial and lateral boundary conditions used in MITgcm have been chosen in order to render it a one-way nested model of the POM simulation. MITgcm uses the same initial condition used in POM. Moreover, the two-way exchange through the strait is achieved by laterally forcing the model through the imposition of the mean baroclinic velocities and tracers extracted from the POM simulation. Tidal forcing was introduced by prescribing at the open boundaries the main diurnal (O_1, K_1) and semidiurnal (M_2, S_2) barotropic tidal currents (depth-averaged currents), always extracted from POM.

Wave reflections at the open boundaries are minimized by adding a Newtonian relaxation term to the tracer equations within the boundary area and implementing the flow relaxation scheme proposed by *Carter and Merrifield* [2007] for the velocity field. For consistency with POM, the same spin-up phase has been followed in the MITgcm simulation. As for Exp-POM, after this spin-up phase the MITgcm was run for a further tropical month (27.321 days) that represents our reference experiment (Exp-MIT). Here we stress that by construction, MITgcm represents a one-way nested model for the POM simulation.

3.3. MODELS VALIDATION

The simulation performed with POM has been validated against most of the available *in situ* data by *Sanchez-Roman et al*. [2009] and *Sannino et al*. [2009a]. *Sanchez-Roman et al*. [2009] compared the predicted and observed amplitude and phase of the diurnal and semidiurnal tidal components of the along-strait velocity field at different depths; the results were considered satisfactory with differences limited in most parts of the strait to less than 10 cm s^{-1} in amplitude and 20° in phase. Moreover, comparing the predicted and observed amplitude and phase of the semidiurnal tidal components of the surface elevation, *Sannino et al*. [2009a] found that the maximum differences did not exceed 3.6 cm in amplitude (with a maximum error that did not exceed 18%) and 11° in phase.

Provided that the MITgcm model is a nested model of the POM simulation, barotropic tidal currents are similar in both models, except for small differences attributed to finer resolution and better representation of the bottom topography of the nested model. Table 3.1 shows results of harmonic analysis applied to barotropic velocity (depth-averaged) time series at ES (35°51.7′N, 5°58.6′W), CS (35°54.8′N, 5°44.7′W), TN (35°57.6′N, 5°33.0′), and GIB (35°59.7′N, 5°22.7′W). Differences between velocity amplitudes are 12.9 ± 8.2%, whereas tidal phases differ in 26.3 ± 10.5°. As expected, both models reproduce fairly similar barotropic tides, which in turn are in good agreement with *in situ* data. Despite the good agreement

Table 3.1 Tidal amplitudes and phases of barotropic currents simulated by the nesting (POM) and nested (MITgcm) models at ES (35°51.7′N, 5°58.6′W), CS (35°54.8′N, 5°44.7′W), TN (35°57.6′N, 5°33.0′), and GIB (35°59.7′N, 5°22.7′W).

Tidal Const.	ES	CS	TN	GIB
Amplitude POM				
M_2	56.74 ± 0.32	107.55 ± 1.08	60.96 ± 1.16	38.76 ± 0.51
S_2	20.88 ± 0.35	38.87 ± 1.28	22.20 ± 1.33	13.57 ± 0.60
K_1	12.08 ± 0.26	23.13 ± 0.55	12.12 ± 0.22	7.05 ± 0.24
O_1	14.20 ± 0.30	26.18 ± 0.50	13.26 ± 0.22	7.86 ± 0.23
Amplitude MITgcm				
M_2	56.97 ± 0.23	114.51 ± 0.38	54.56 ± 0.41	42.87 ± 0.39
S_2	20.54 ± 0.22	42.41 ± 0.41	18.83 ± 0.38	15.02 ± 0.30
K_1	9.33 ± 0.14	22.16 ± 0.34	10.15 ± 0.43	6.10 ± 0.23
O_1	11.11 ± 0.15	24.00 ± 0.35	10.34 ± 0.47	6.25 ± 0.27
Phase POM				
M_2	116.6 ± 0.3	117.1 ± 0.6	107.7 ± 1.1	114.9 ± 0.8
S_2	199.7 ± 0.9	198.0 ± 1.8	191.7 ± 2.9	195.0 ± 2.5
K_1	18.6 ± 1.4	6.5 ± 1.2	359.9 ± 1.1	357.9 ± 1.8
O_1	198.1 ± 1.2	184.3 ± 1.2	179.3 ± 0.1	174.9 ± 1.7
Phase MITgcm				
M_2	136.1 ± 0.2	136.8 ± 0.2	129.7 ± 0.4	127.9 ± 0.4
S_2	168.0 ± 0.7	168.7 ± 0.6	162.9 ± 1.3	161.4 ± 1.6
K_1	358.9 ± 0.9	354.9 ± 0.9	348.1 ± 2.5	336.6 ± 2.4
O_1	237.1 ± 0.9	227.3 ± 0.8	221.5 ± 2.5	210.7 ± 2.3

between MITgcm and POM barotropic tides, baroclinic tides present significant differences. As it will be shown in the next section, the fine resolution and nonhydrostatic formulation of MITgcm make the model capable of accurately resolving the generation and evolution of internal tides, including short internal lee waves generated near bottom obstacles, and propagating solitary waves of large amplitude, some of the most striking phenomena observed in the SoG [*Lacombe and Richez*, 1982].

3.4. RESULTS

In this section, the SoG circulation as simulated by the two models will be compared in terms of internal bore evolution, three-layer characteristics, and hydraulics.

3.4.1. Internal Bore Evolution

One of the most noticeable phenomena observed in the SoG is represented by the propagating internal tidal wave generated over CS. At its leading edge, the internal tide can be characterized as a tidal bore: a train of internal waves of about 100 meters amplitude and 1 km wavelength [*Garrido et al*., 2008; *Lacombe and Richez*, 1982]. Figures 3.3 and 3.4 display the evolution of the salinity and velocity fields from the midstage of the flood tide to the midstage of the ebb tide of a tidal cycle as simulated by the POM and MITgcm model, respectively. The comparison of the two figures reveals important differences between the two models. In a late stage of the flood tide, POM exhibits two steep depressions of the isohalines at the lee side of ES and CS (Figures 3.3a, b). As discussed by *Sannino et al*. [2009a], these two internal features constitute two internal hydraulic jumps. The hydraulic jump at ES is quasi-permanent, whereas the one at the lee side of CS is intermittent since hydraulic control is lost in the majority of tidal cycles when barotropic tidal flow reverses. This occurs in panel 3c, which shows the release of the hydraulic jump toward the Mediterranean. Since nonhydrostatic effects are missing in POM, the moving hydraulic jump (or internal bore) cannot undergo its classical evolution into a series of short solitary waves as predicted by weakly nonlinear theories. The internal bore may only give rise to a shock wave since only the weak dispersion introduced by Earth's rotation, unable to balance the steepening effect of nonlinearity, is at work. Consequently, the baroclinic field beyond CS has to be considered unrealistic.

For the nonhydrostatic simulation (Figure 3.4), barotropic forcing produces, at first glance, the same overall picture with a double internal hydraulic jump at the lee side of ES and CS but with much better resolved fine baroclinic structures. Tangier Basin and the lee side of ES appear as places where short unsteady waves develop (Figures 3.4a–c). Further analysis of the baroclinic field reveals that in addition to the hydraulic jump located at the lee side of CS, another internal bore is generated upstream of the sill, just over the leading edge of CS crest. This bore is released with the relaxation of the barotropic flow evolving into a succession of internal solitary waves of depression (see *Garrido et al*., 2012, for an exhaustive analysis). Figure 3.5 shows the baroclinic velocity field (along-strait component) reproduced by the two models across the internal wave train (see grey contour in Figures 3.3d and 3.4d). Baroclinic velocities are calculated as the difference between the total velocity and its barotropic component (depth-average value, which in this case is around 0.6 m/s). Throughout 8 kilometers, the total velocity field is dominated by the orbital velocities of a series of internal solitary waves (Figure 3.5a), which are as large as 1 m/s near the surface and around −0.6 m/s below the pycnocline. Although the magnitudes of velocity are similar, the velocity field is much coarser, and the countercurrent below 150-m depth is significantly underestimated. Differences in the vertical component of velocities are much more dramatic (Figures 3.5c, d).

As expected, vertical velocities associated with internal solitons are as large as 0.3 ms^{-1}, more than three times larger than those reproduced by the σ-coordinate model.

3.4.2. Three-layer definition and properties

As argued by *Bray et al*. [1995] and subsequently verified by *Sannino et al*. [2009a], the two-way exchange in the SoG is best represented by a three-layer system composed of an upper layer of Atlantic water, a lower layer of saltier and colder Mediterranean water, and an interface layer in between.

The same method applied in *Sannino et al*. [2009a] for classifying all salinity profiles as Atlantic layer (AL), interface layer (IL), and Mediterranean layer (ML) has been used for analyzing the MITgcm simulation. In particular, following *Bray et al*. [1995] the upper and lower limit of the halocline have been chosen as the upper and lower limits of the interface layer. Figure 3.6 shows the time-averaged thicknesses of the three layers together with the depth of the midpoint of the interface layer as obtained for MITgcm. By comparing such figure with the equivalent figure obtained for POM (see Figure 16 in *Sannino et al*. [2009a]), it appears that the main patterns are similar. However, the thickness of the AL is systematically larger in MITgcm than in POM, with values ranging from about 60 m west of CS to about 20 m along TN (Figure 3.7). Note that the difference along TN in terms of percentage of the MITgcm AL thickness is 100%. Such values are reached far from the coast; there POM exceeds MITgcm. The opposite behavior close to the coast is due to the different representation of the coastal bathymetry in the two models.

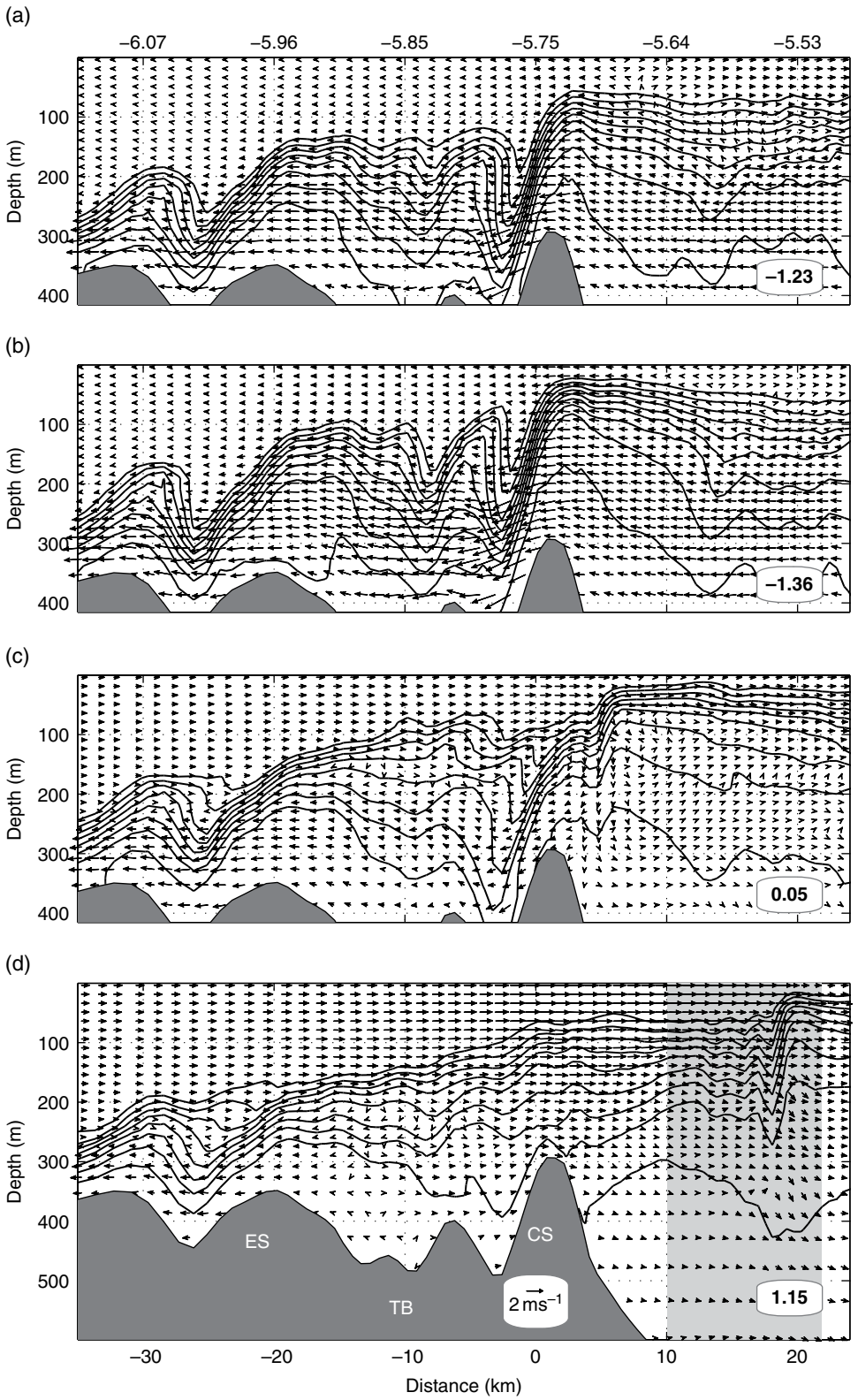

Figure 3.3 Time evolution of isohalines 36.40, 36.65, … , 38.65 and velocity currents simulated by POM during one tidal cycle of moderate tidal strength (Exp-POM). The barotropic velocity (in ms^{-1}) over Camarinal Sill is indicated at the lower right corner of the panels. Elapse times after (panel a) are 1:40 h (panel b), 4:40 h (panel c), and 7:00 h (panel d).

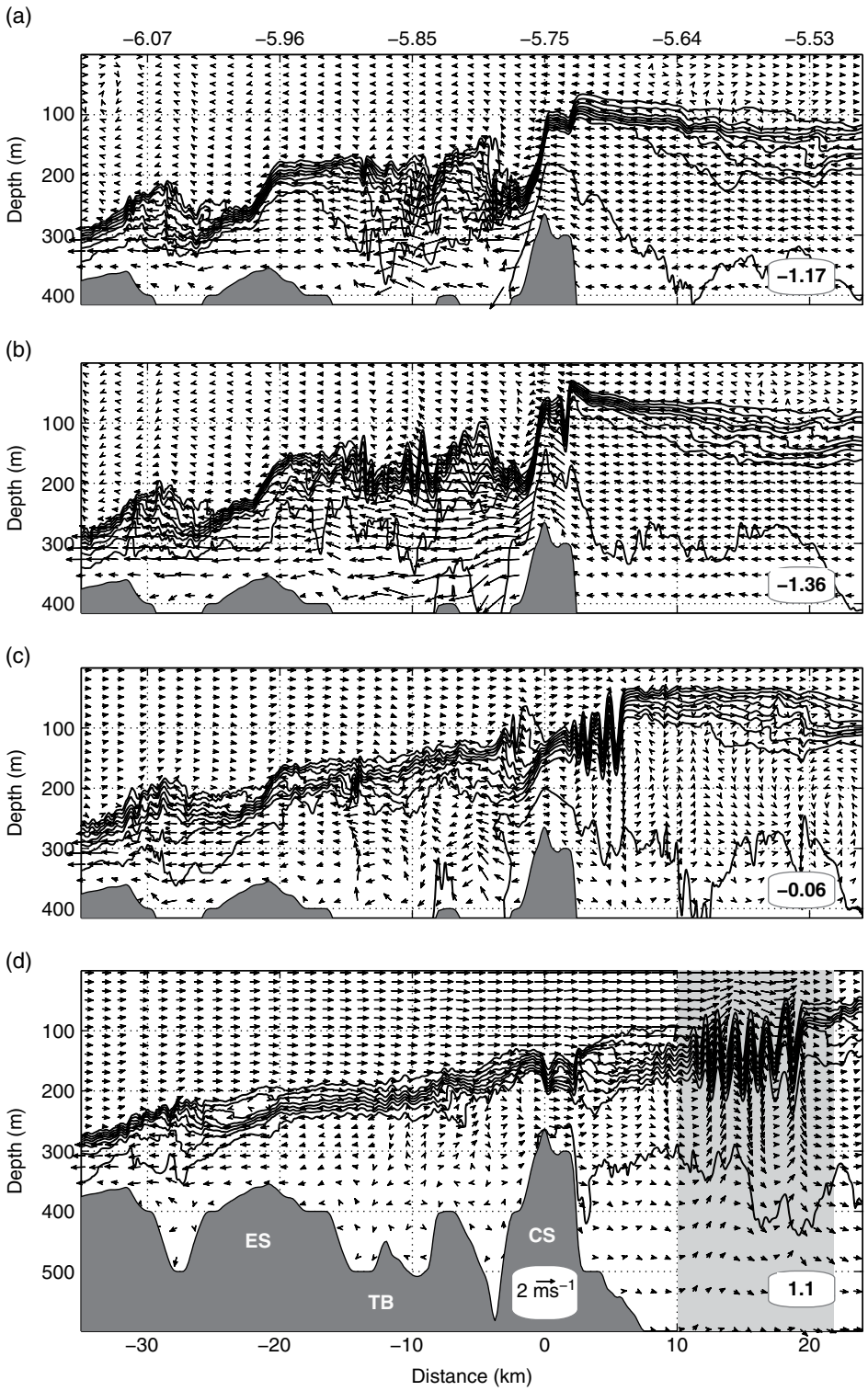

Figure 3.4 Same as Figure 3.3, using output from the MITgcm model (Exp-MIT).

As shown in Figure 3.8, POM bathymetry is systematically deeper than MITgcm. As for AL, the thickness of the ML is systematically higher in MITgcm than in POM (between 50 and 150 m), with some exceptions close to the northern coast, again due to the different representation of the bathymetry. The increased thickness for both the AL and ML in the MITgcm simulation implies a general reduction of the interface layer thickness with respect to

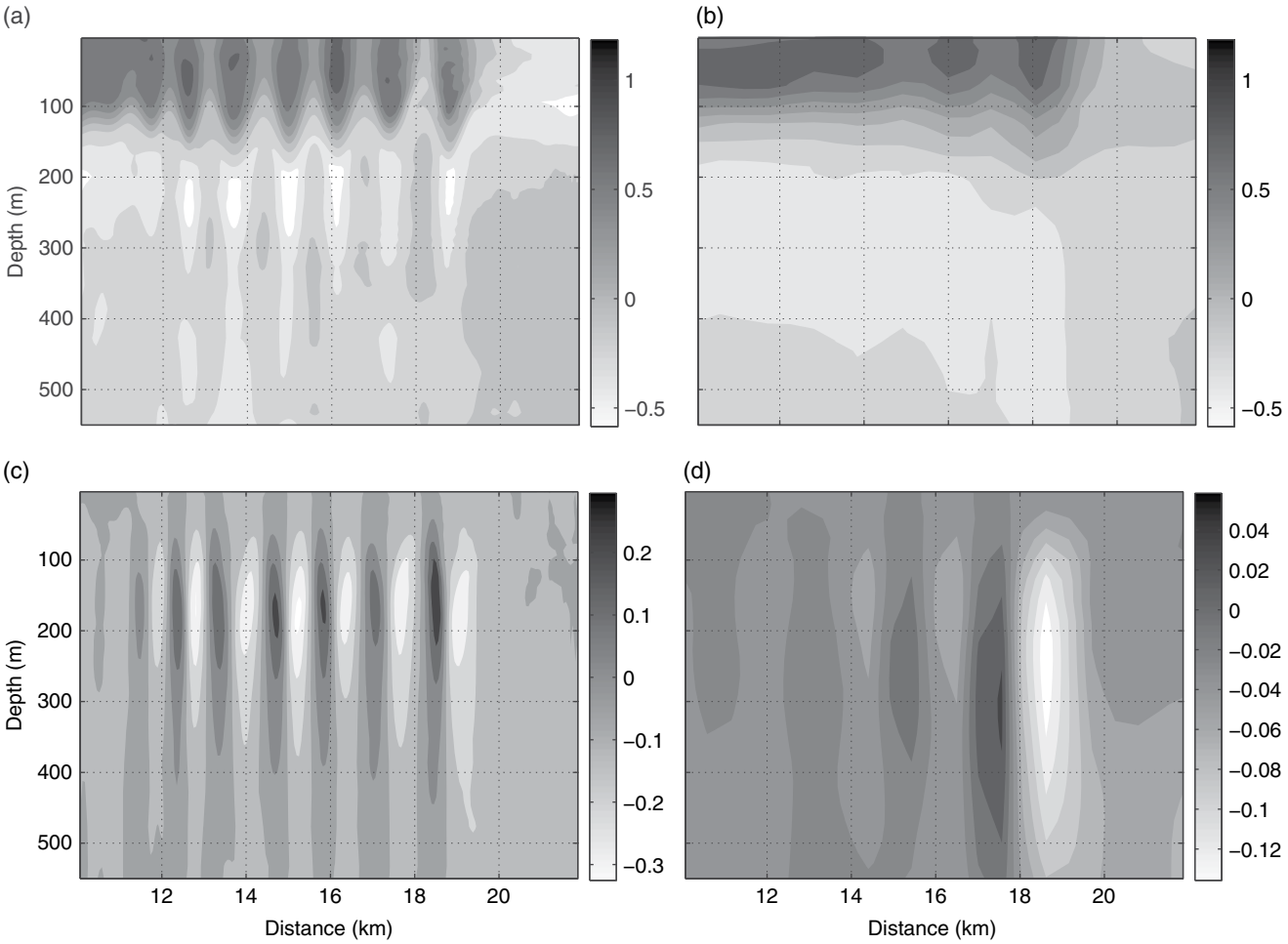

Figure 3.5 (a) Baroclinic horizontal velocity simulated by MITgcm during the arrival of an internal waves train at TN (see shaded rectangle in Figure 3.3d); (b) Same as (a) simulated by POM; (c) Vertical current simulated by MITgcm during the same instant of (a); (d) Same as (c) simulated by POM.

POM. Such reduction is more evident west of CS, along TB, and west of ES. The only exception occurs confined in the area near the northern coast of TN where the MITgcm predicts a thicker layer. Such difference is again attributed to the different representation of the bathymetry.

However, there is a good agreement between the mid-point interface depth simulated by POM and MITgcm (Figure 3.6). The differences hardly exceed 20 m, and are confined to points where the bathymetry disagrees.

Comparison of the two model results with those obtained by *Bray et al.* [1995] (Figure 6 in *Bray et al.* [1995]) shows good agreement with MITgcm whereas POM systematically overestimates the interface thickness. This difference can be attributed to the excess of spurious diapycnal mixing produced by POM that overshadows the naturally occurring mixing. The systematic spreading of the isohalines along the SoG (Figure 3.3) is additional evidence of such a strong diapycnal mixing affecting the POM simulation.

The different layer thicknesses have a direct effect on the water transport. For the MITgcm, the resulting transports for the three layers over the tropical month period are shown in Figure 3.9 for four different cross-strait sections located at ES, CS, Tarifa, and Gibraltar, respectively (sections A, B, C, and D in Figure 3.2). The Atlantic (*ALT*), interface (*ILT*), and Mediterranean layer transport (*MLT*) have been computed as in *Sannino et al.* [2009a], that is:

$$ALT(x,t) = \int_{y_{S1}(x)}^{y_{N1}(x)} \int_{dw_1(x,,y,,t)}^{up_1(x,,y,,t)} u(x,y,z,t)dzdy \qquad (3)$$

$$ILT(x,t) = \int_{y_{S2}(x)}^{y_{N2}(x)} \int_{dw_2(x,,y,,t)}^{up_2(x,,y,,t)} u(x,y,z,t)dzdy \qquad (4)$$

$$MLT(x,t) = \int_{y_{S3}(x)}^{y_{N3}(x)} \int_{dw_3(x,,y,,t)}^{up_3(x,,y,,t)} u(x,y,z,t)dzdy, \qquad (5)$$

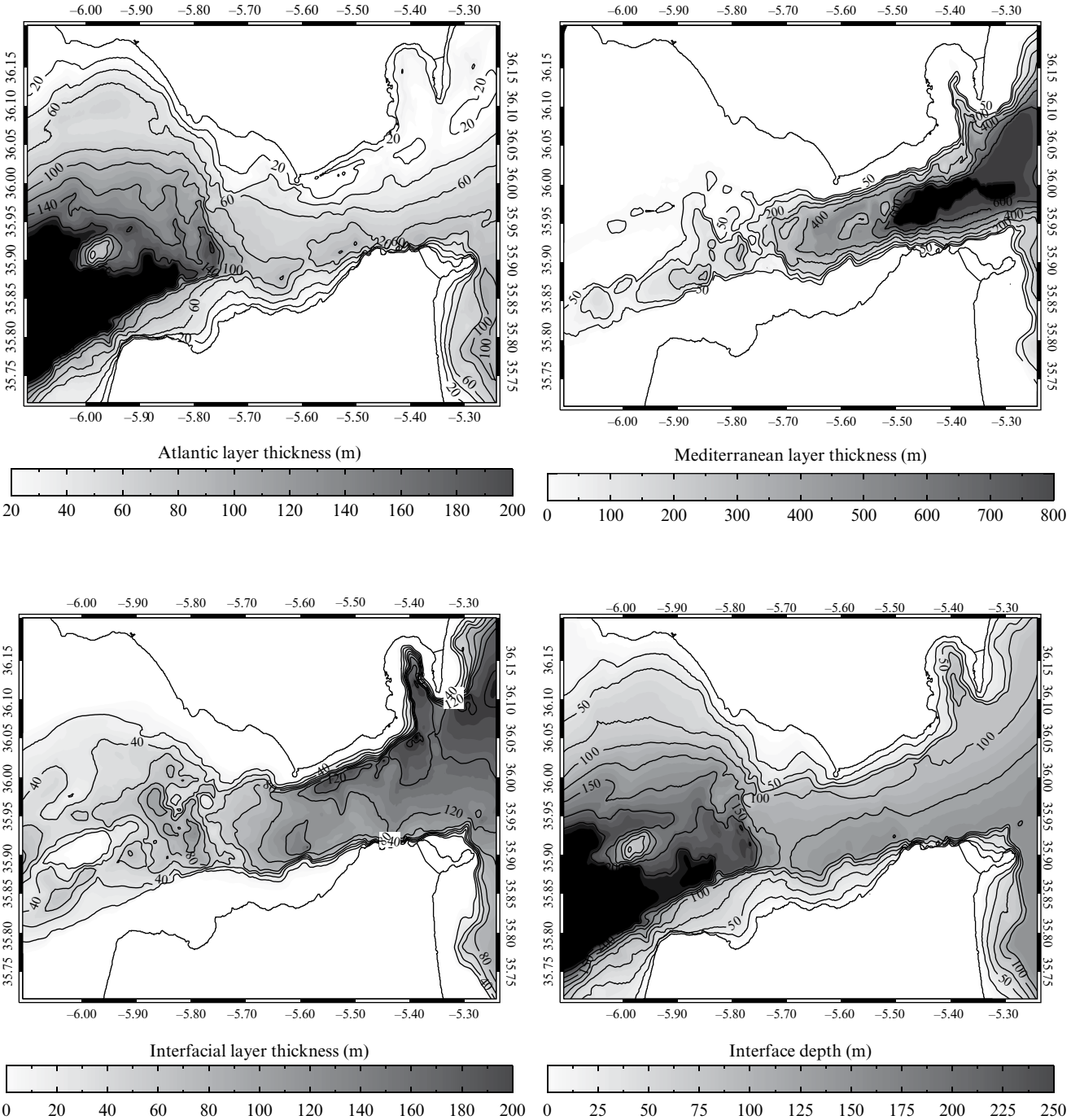

Figure 3.6 Time-averaged Atlantic, interface, and Mediterranean layer thickness, and depth of the midpoint of the interface layer as simulated by the MITgcm numerical model (Exp-MIT).

where up_n and dw_n are the instantaneous depths of the upper and lower bounds of the nth layer, while y_{Sn} and y_{Nn} represent the southern and northern limit of the cross section x and nth layer.

Figure 3.9 shows that the Atlantic layer carries water eastward with a small fraction of the transport periodically directed in the opposite direction. This small fraction reduces progressively from west to east, becoming null after crossing CS. An opposite behavior is exhibited by *MLT* where the principal direction is westward, and the eastward fraction reduces gradually from section D to section A where it is reduced to zero. *ILT* is comparable with *MLT* (*ALT*) transport at the western (eastern) side of the strait, but never exceeds the Atlantic or

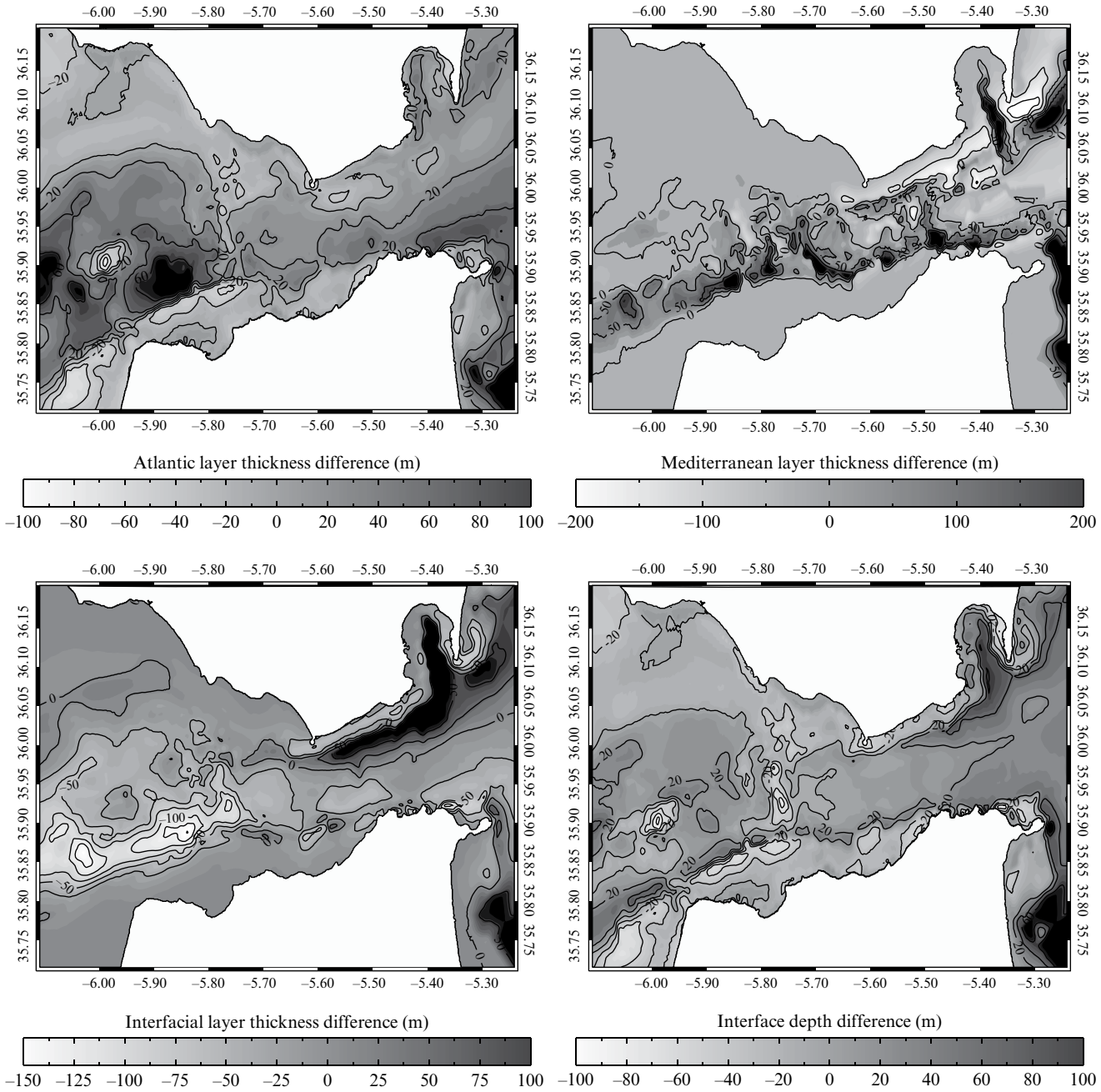

Figure 3.7 Difference MITgcm-POM for the time-averaged Atlantic, interface, and Mediterranean layer thickness, and depth of the midpoint of the interface layer.

Mediterranean contribution. This is an important difference with respect to the results obtained by *Sannino et al*. [2009a] where the interface layer transport was about two times larger than the Mediterranean over Espartel Sill, and three times larger than the Atlantic at the eastern limit of the SoG (see Figure 18 of *Sannino et al*. [2009a]).

3.4.3. Hydraulics

A long-standing question about the SoG concerns whether, and to what extent, the narrows and the two major sills hydraulically control the exchange flow. *Armi and Farmer* [1988] provide a detailed 2-D, two-layer system analysis of control locations based on observations

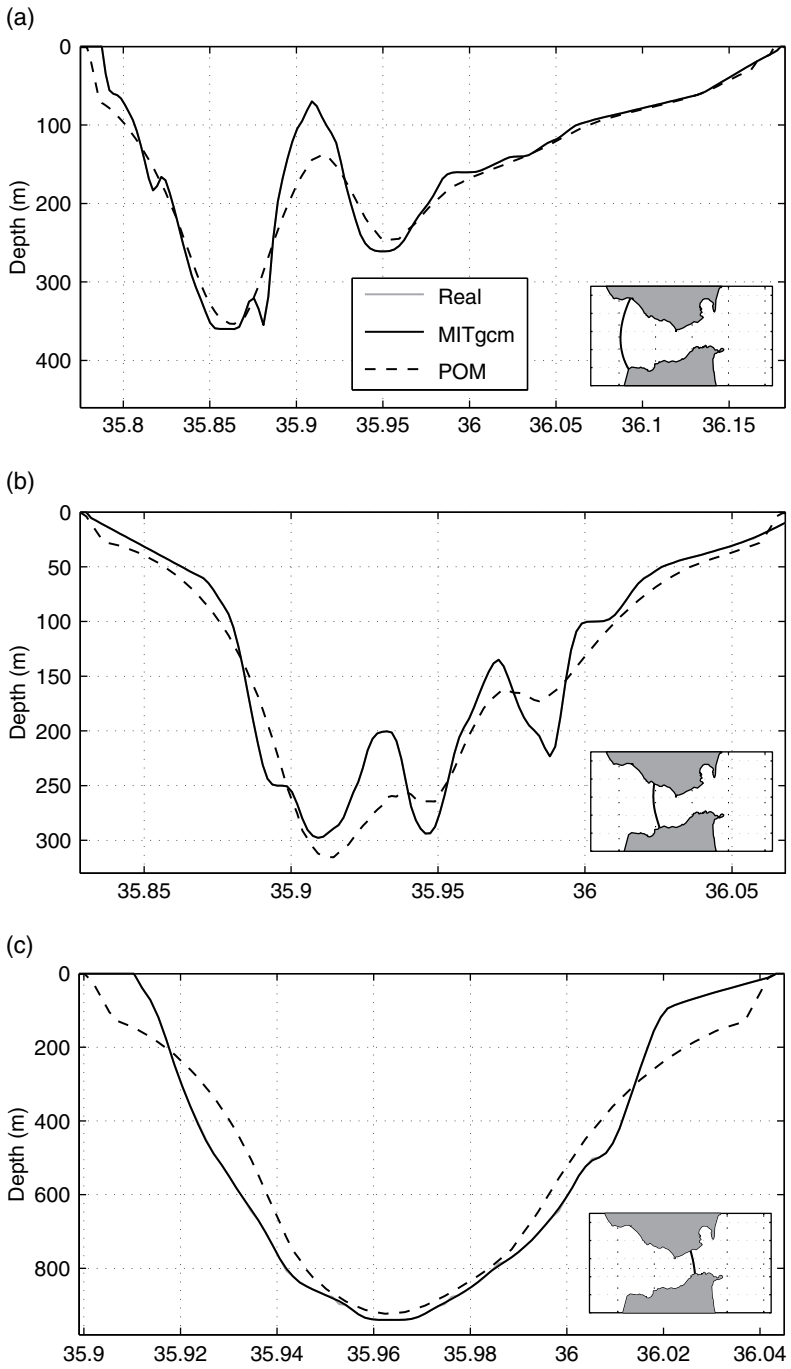

Figure 3.8 Original bottom topography (gray line) representation by partial cells (black solid line), and representation by σ-levels (dashed line) at (a) Espartel cross section, (b) Camarinal cross section, and (c) Tarifa Narrows cross section. Note that the actual partial cell representation fits perfectly the original bottom topography.

taken along or near the strait center line. They observed two permanent controls: one located at ES and the second within TN. The location of the control along TN is modified by the eastward propagating bore released at CS. They observed also a periodic control at CS due to the tidal action. The existence of two permanent controls would imply maximal exchange between the Atlantic and Mediterranean and overmixing within the Mediterranean. *Sannino et al*. [2009a] attempted to verify these conclusions by undertaking careful assessment of the hydraulic conditions at various sections of the SoG based on a three-layer representation of the flow with transversally varying velocity within each layer.

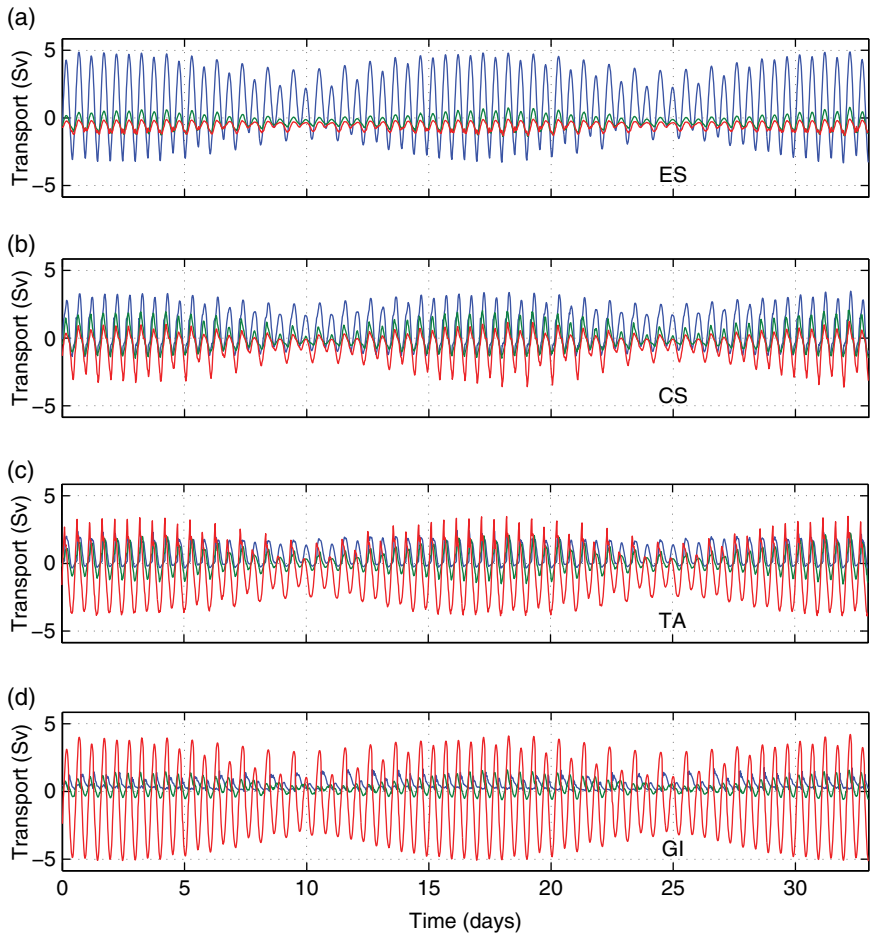

Figure 3.9 (a) Time evolution of Atlantic layer transport (blue line), interfacial-mixed layer (green line), and Mediterranean layer transport (red line) at Espartel section; (b) Same as (a) for Camarinal Sill section; (c) Same as (a) for Tarifa section; (d) Same as (a) for Gibraltar section. For color detail, please see color plate section.

We now examine the extent to which their conclusions are supported by MITgcm. The three-layer formulation was undertaken because of uncertainties about where, in two-layer formulation, the interface is to be located. (Episodic controls are located at ES and CS.) The existence of two permanent controls would imply maximal exchange between the Atlantic and Mediterranean and overmixing within the Mediterranean. *Sannino et al.* [2009a] attempted to verify these conclusions by undertaking careful assessment of the hydraulic conditions at various sections of the SoG based on a three-layer representation of the flow with transversally varying velocity within each layer.

We now further examine the extent to which their conclusions are supported by MITgcm. As discussed in *Sannino et al.* [2009a] and *Pickart et al.* [2010], the linear long waves of the three-layer system are associated with two vertical modes akin to the first and second baroclinic modes of a continuously stratified system. There are two waves for each mode and, in the absence of background flow, the two waves propagate in opposite directions. In the presence of weak background velocity, this situation continues to hold, and we say that the flow is subcritical with respect to each mode. If the velocity in one or more layers increases, the flow may become critical, meaning that the phase speed of one of the waves of a particular mode is brought to zero. The condition for critical flow is (see Figure 3.10):

$$\tilde{F}_1^2+\left(\frac{1-r}{r}+\frac{w_3}{w_2}\right)\tilde{F}_2^2+\tilde{F}_3^2-\frac{w_3}{w_2}\tilde{F}_1^2\tilde{F}_2^2 -\tilde{F}_1^2\tilde{F}_3^2-\frac{1-r}{r}\tilde{F}_2^2\tilde{F}_3^2=1, \tag{6}$$

where

$$\tilde{F}_1^2=\left(\frac{1}{w_2}\int_{y_1L}^{y_1R}\frac{g'_{21}H_1}{u_1^2}dy_1\right)^{-1},\ \tilde{F}_2^2=\left(\frac{1}{w_2}\int_{y_2L}^{y_2R}\frac{g'_{32}H_2}{u_2^2}dy_2\right)^{-1},$$
$$\tilde{F}_3^2=\left(\frac{1}{w_3}\int_{y_3L}^{y_3R}\frac{g'_{32}H_3}{u_3^2}dy_3\right)^{-1}, \tag{7}$$

$g'_{21} = g(\rho_2 - \rho_1)/\bar{\rho}$, $g'_{32} = g(\rho_3 - \rho_2)/\bar{\rho}$, $r = \dfrac{\rho_2 - \rho_1}{\rho_3 - \rho_1}$ and w_n is the width of the interface overlying layer n. Note that $\tilde{F}_1^2$, $\tilde{F}_2^2$, and $\tilde{F}_3^2$ are generalized versions of layer Froude numbers and cannot be thought of as ratios of intrinsic to advection speeds.

When the speed of one or more layers is increased, the two waves belonging to a particular mode may move in the same directions, in which case we say that the flow is supercritical with respect to that mode. The connection with traditional hydraulics maybe clouded by the fact that the phase speeds can be complex, and *Sannino et al.* [2009a] therefore use the terms *provisionally subcritical* and *provisionally supercritical* to describe the appropriate regimes. This caveat is to be understood in what follows, so we will drop the modifier *provisional*.

The object of the hydraulic analysis is to map out regions of subcritical and supercritical flow along with the location control sections. There the flow is critical, equation 6 is satisfied, and a transition between regimes exists. To distinguish between states that are critical with respect to the first, as opposed to second, internal mode, one can evaluate the sign of

$$\alpha = \frac{w_2}{w_3 \tilde{F}_2^2}\left[\frac{r}{1-r}\left(\tilde{F}_1^2 - 1\right) + \tilde{F}_2^2\right],$$

which gives the ratio of the lower to upper interface displacements due to the wave. If α is negative, the flow is classified as controlled for the second baroclinic mode. On the contrary, a positive α indicates criticality for the first mode. The remaining case occurs when both negative and positive α are possible. Such a situation is classified as two-modes controlled (see *Garrido et al.* [2012] for a rigorous derivation).

Figure 3.11 shows the frequency of occurrence, over the tropical month period, of supercritical flow with respect to only one mode (Figure 3.11 intermediate panel), and both modes (Figure 3.11 upper panel) along

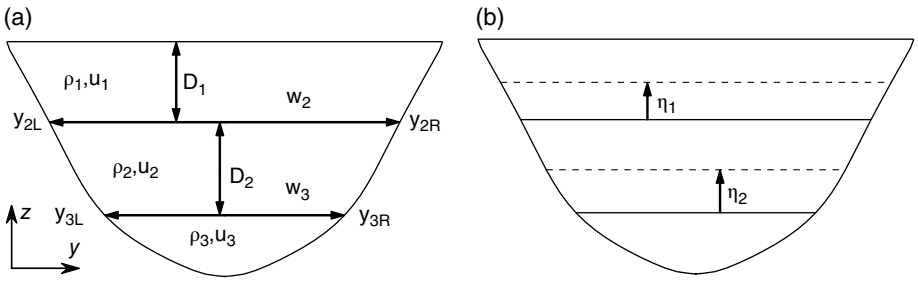

Figure 3.10 Definition sketch for a three-layer flow.

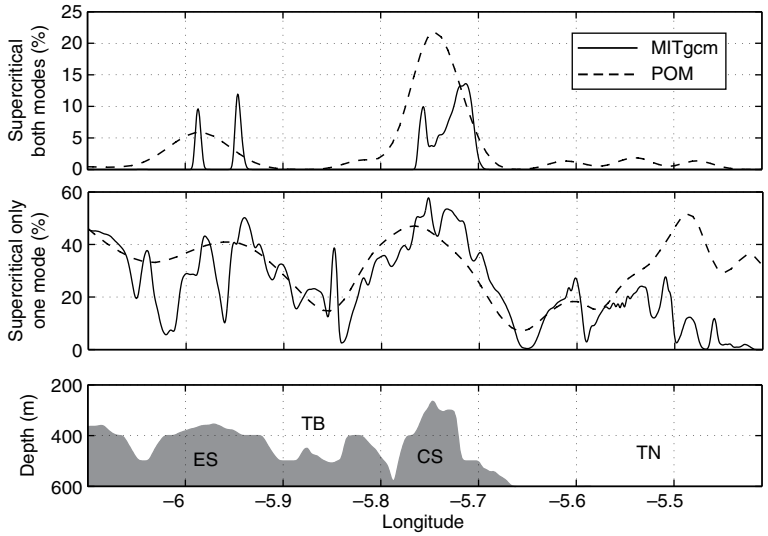

Figure 3.11 Frequency of occurrence, over the tropical month period, of supercritical flow with respect to bath modes (upper panel) and one mode (intermediate panel) along the strait as obtained by POM (dashed line) and MITgcm (solid line). Lower panel shows the bottom topography along the central axis of the strait.

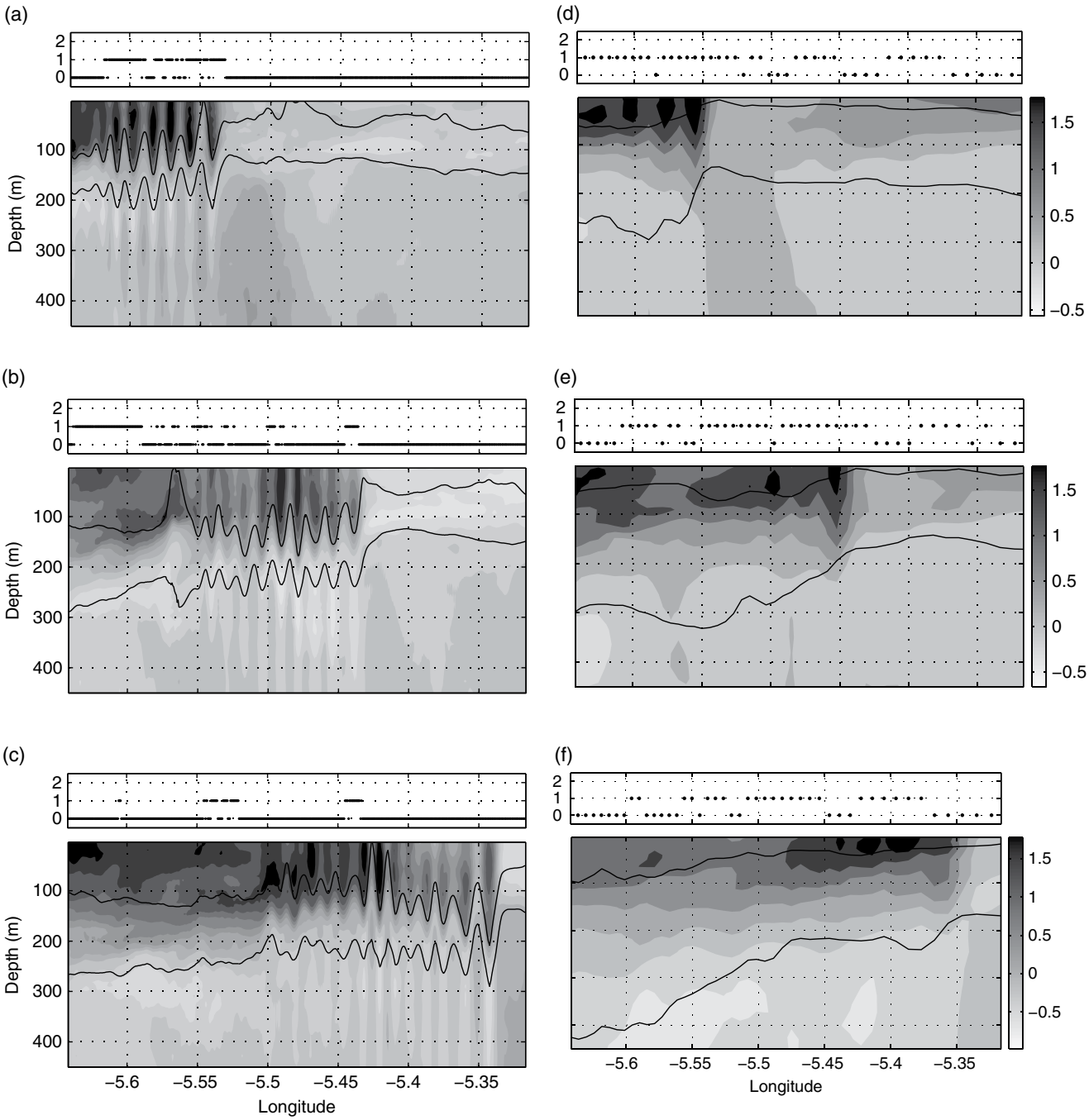

Figure 3.12 Evolution of the horizontal velocity field along longitudinal Section E (See Figure 3.2) during the arrival of an internal wave train to TN. Thick solid lines indicate the layer interfaces in the three-layer system. The sequence corresponds to the 13th day of simulation. Elapse time between upper and lower frames is 1.33 hours. Panels on the top of each frame indicate the flow criticality; zero: subcritical flow; one: only one internal mode controlled; two: both internal modes controlled. Left panels are for MITgcm, while right panels are for POM.

the strait as obtained by POM and MITgcm. Note that in both models the flow is much more prone to be supercritical with respect to only one mode. Moreover, for both models we observe that over CS and ES the flow criticality displays its maximum frequency.

That being said, some differences between the two models are still evident. In general, MITgcm displays a marked along-strait variability related to the finer description of the bathymetry. Moreover, when both modes are supercritical, MITgcm predicts lower values all along the

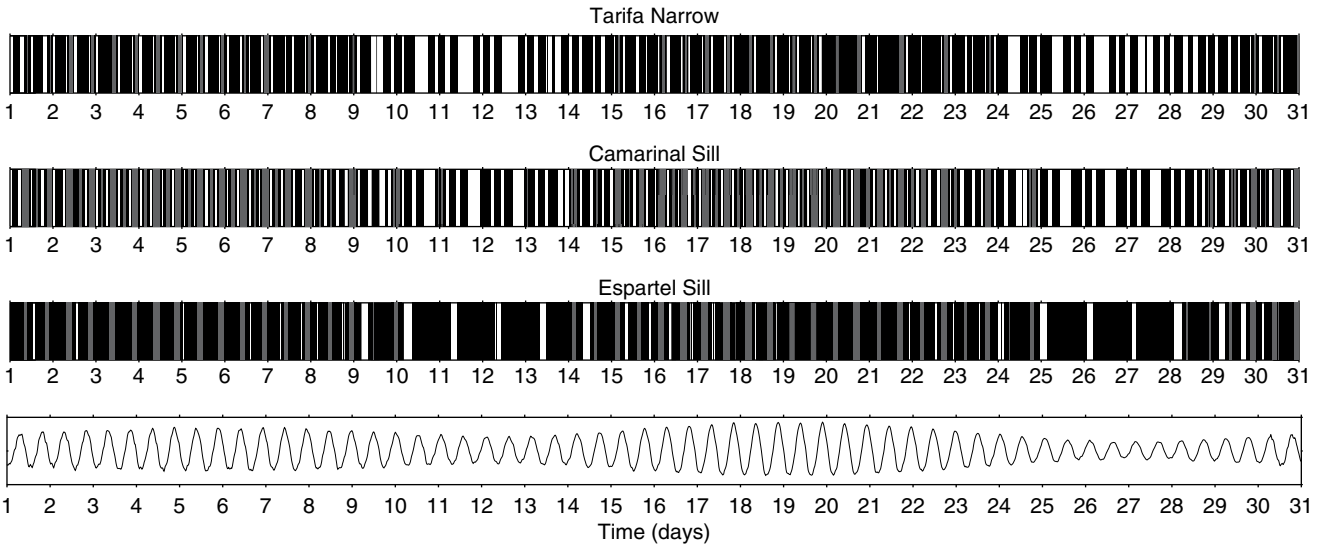

Figure 3.13 Bars indicating the presence of provisional supercritical flow as simulated by MITgcm with respect to one mode (black), and with respect to both modes (gray) in the three main regions of the strait: (from top) Tarifa Narrow, Camarinal Sill, and Espartel Sill; (bottom panel) time reference referred to the tidal elevation at Tarifa.

strait compared to POM, except for ES where MITgcm exceeds POM. When the flow is supercritical with respect to just one mode, the major differences are confined along TN. In particular, POM predicts higher frequencies compared to MITgcm. Due to the importance that a control in TN can play in determining the final hydraulic regime reached in the SoG, it is interesting to analyze in detail such differences.

Figure 3.12 shows the evolution of a bore through TN as simulated by MITgcm and POM. The bore propagation is presented as a temporal sequence of three along-strait velocity fields. To highlight the shape and position of the bore, two black lines representing the upper and lower bound of the interface thickness have been superimposed. The related hydraulic control is also indicated in each figure. As shown before, the upper layer is systematically thinner in POM, while the interface layer is thinner in MITgcm. Such differences, together with differences in the velocity fields, lead to the determination of different hydraulic behavior. POM predicts a quasi-permanent supercritical flow. East of the bore the velocity of the AL in POM is systematically higher than in MITgcm. In contrast to POM, MITgcm achieves the control only when the eastward bore is present in TN.

For a complete understanding of the hydraulic regimes in terms of maximal and submaximal exchange, the simultaneous presence of supercritical flow regions through the strait have to be explored. As in *Sannino et al*. [2009a], the three most likely regions of CS, ES, and TN will be analyzed. In Figure 3.13 a bar-plot similar to Figure 19 of *Sannino et al*. [2009a] shows the evolution of the hydraulic control in these three regions according to MITgcm. Black bars indicate the presence of supercritical flow with respect to only one mode, while gray bars are used when the flow is supercritical with respect to both modes. The frequency of appearance of supercritical flow, with respect to one and both modes, over the entire tropical month period is about 46%, 73%, and 92% at TN, CS, and ES, respectively.

Moreover, while the flow is supercritical with respect to both modes for only 4% in TN, the percentage increases up to 30% at CS. A slightly lower percentage is found at ES. Thus, while at CS the flow is supercritical with respect to one and both modes with approximately the same percentage, the flow is principally controlled with respect to only one mode both at TN and ES. Similar percentages for both modes controlled were found also by *Sannino et al*. [2009a]. On the contrary, comparing the values obtained when only one mode is controlled, it appears that the percentage for TN has undergone a substantial reduction with respect to *Sannino et al*. [2009a] (from 70% to 42%); a more limited reduction occurs at ES (from 74% to 62%); and a similar value is obtained for CS (from 41% to 48%).

In conclusion, the hydraulic control section in TN, deemed necessary for maximal exchange conditions in the *Armi and Farmer* [1988] model, occurs with a significantly lower frequency in the MITgcm. If one requires that both modes be supercritical, which would correspond to supercritical flow in their two-layer model, the percentage of time over which control occurs in TN (grey bars in Figure 3.13) is quite low. It would therefore appear that maximal control is largely expunged within the MITgcm.

Table 3.2 Main characteristics and parameterizations used for the seven experiments performed.

	Model	Model grid	Non-hydrostatic	Vertical diffusivity	Horizontal diffusivity	MPDATA iterations
Exp-POM	POM	$362 \times 53 \times 32$	NO	*Mellor and Yamada* [1982]	TPRNI =1	3
EXP1	POM	$362 \times 53 \times 32$	NO	Null	TPRNI =1	3
EXP2	POM	$362 \times 53 \times 32$	NO	Null	TPRNI =1	5
EXP3	POM	$362 \times 53 \times 32$	NO	Null	TPRNI =0	5
Exp-MIT	MITgcm	$1440 \times 210 \times 53$	YES	*Pacanowski and Philander* [1981]	Laplacian: $1 \cdot 10^{-2}$ $m^2\ s^{-1}$	Not present in MITgcm
EXP4	MITgcm	$1440 \times 210 \times 53$	NO	*Pacanowski and Philander* [1981]	Laplacian: $1 \cdot 10^{-2}$ $m^2\ s^{-1}$	Not present in MITgcm
EXP5	MITgcm	$362 \times 53 \times 46$	NO	*Pacanowski and Philander* [1981]	Laplacian: $1 \cdot 10^{-2}$ $m^2\ s^{-1}$	Not present in MITgcm

3.4.4. Sensitivity Experiments

A set of five additional sensitivity experiments was carried out. Three experiments were conducted to investigate the origin of diapycnal mixing present in the POM simulation. The fourth experiment was performed to evaluate the impact of the nonhydrostaticity on the simulated hydraulic regime. Finally, another experiment was carried out to examine the influence of the horizontal and vertical resolution on the simulated exchange flow. In Table 3.2 are reported the main model characteristics and parameterizations used for the entire set of experiments.

3.4.4.1. Advection and diapycnal mixing The reference experiment (Exp-POM) is first repeated with the parameter controlling vertical diffusivity (KH in *pom*98) set to zero (EXP1). In the second experiment (EXP2), KH remains zero and the number of corrective iterations of the MPDATA advection scheme is increased from three to five. The third experiment (EXP3) is the same as EXP2 except that the horizontal diffusivity is also set to zero (TPRNI = 0 in *pom*98). A qualitative comparison shows that in EXP1 and EXP2 the spurious diapycnal mixing is only slightly reduced below that of Exp-POM (see Figures 3.14 and 3.15, respectively), whereas a more drastic improvement is obtained in EXP3 (Figure 3.16). These results suggest that the numerically induced mixing is so large in Exp-POM that no additional horizontal diffusivity is needed. Recently, *Marchesiello et al*. [2009] demonstrated that spurious diapycnal mixing can arise from the advection scheme adopted. In particular, they demonstrated that implicit diffusion in diffusive advection schemes, as for example MPDATA, is large enough to produce excessive diapycnal mixing even in high-resolution σ models. We suspect that this is exactly the case.

3.4.4.2. Hydrostatic vs. nonhydrostatic regime To investigate the impact of the nonhydrostaticity on the simulated hydraulic regime, an additional experiment has been performed with MITgcm in which the reference experiment (Exp-MIT) is rerun in hydrostatic mode (EXP4). Figure 3.17 shows the resulting salinity and velocity fields for the midstage of the ebb tide of a tidal cycle of moderate strength obtained for EXP4. Comparison of Figure 3.17 and its nonhydrostatic counterpart (Figure 3.4d), shows that the internal bore is reduced to a simple shock wave when the pressure is rendered hydrostatic. However, such a limitation has no impact on the final simulated hydraulic regime. This can be confirmed through the comparison of the evolution of the hydraulic control along TN as simulated by Exp-MIT (Figure 3.12a, b, c) and EXP4 (Figure 3.18a, b, c), respectively. It is interesting to note that the hydraulic control along TN moves from west to east in a similar way in both experiments. In particular for Exp-MIT, the control in TN is linked to the internal bore, while for EXP4 it is linked to the shock wave.

3.4.4.3. Resolution A further experiment (EXP5) was performed to examine the influence of the horizontal and vertical resolution on the simulated exchange flow (Figure 3.19). In this experiment, Exp-MIT was repeated in hydrostatic mode and with the same horizontal grid as for Exp-POM. In the vertical, the model used 46 unevenly distributed vertical z-levels with decreasing resolution from the ocean surface to the bottom. The first 20 vertical levels are concentrated within the first 300 m of the water column. Model topography is obtained through a bilinear interpolation of the same initial data used for Exp-MIT. Qualitative comparison of simulation with its lower resolution counterpart (Figure 3.19d) shows that higher horizontal resolution has an impact principally on the steepness of the shock wave, which however does not alter the final simulated hydraulic regime. The latter remains very similar to that of EXP4 and consequently to Exp-MIT.

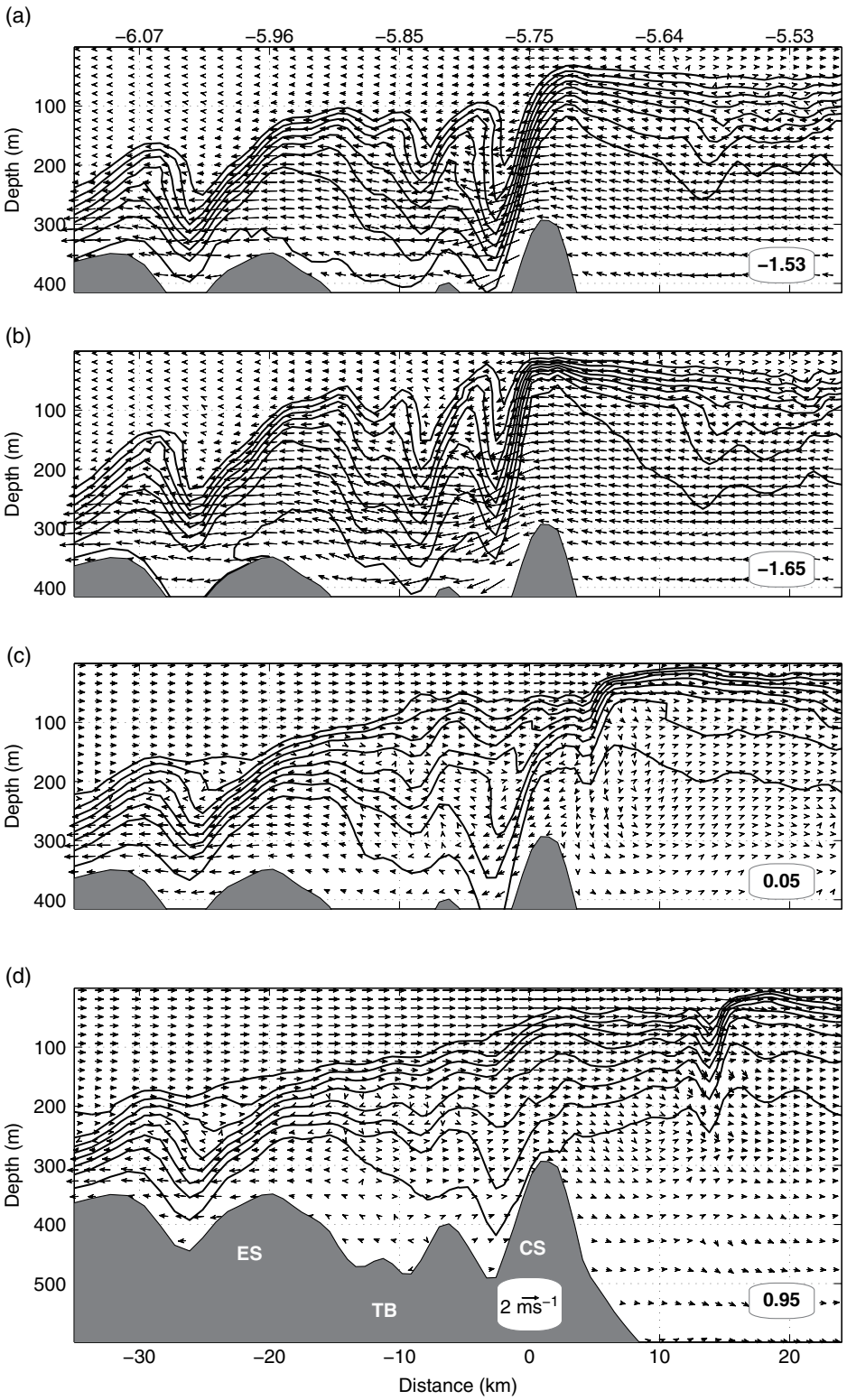

Figure 3.14 Time-evolution of isohalines 36.40, 36.65, … , 38.65 and velocity currents simulated by POM with vertical diffusivity set to zero (EXP1) during one tidal cycle of moderate tidal strength. The barotropic velocity (in ms^{-1}) over Camarinal Sill is indicated at the lower right corner of the panels. Elapse times after (panel a) are 1:40 h (panel b), 4:40 h (panel c), and 7:00 h (panel d).

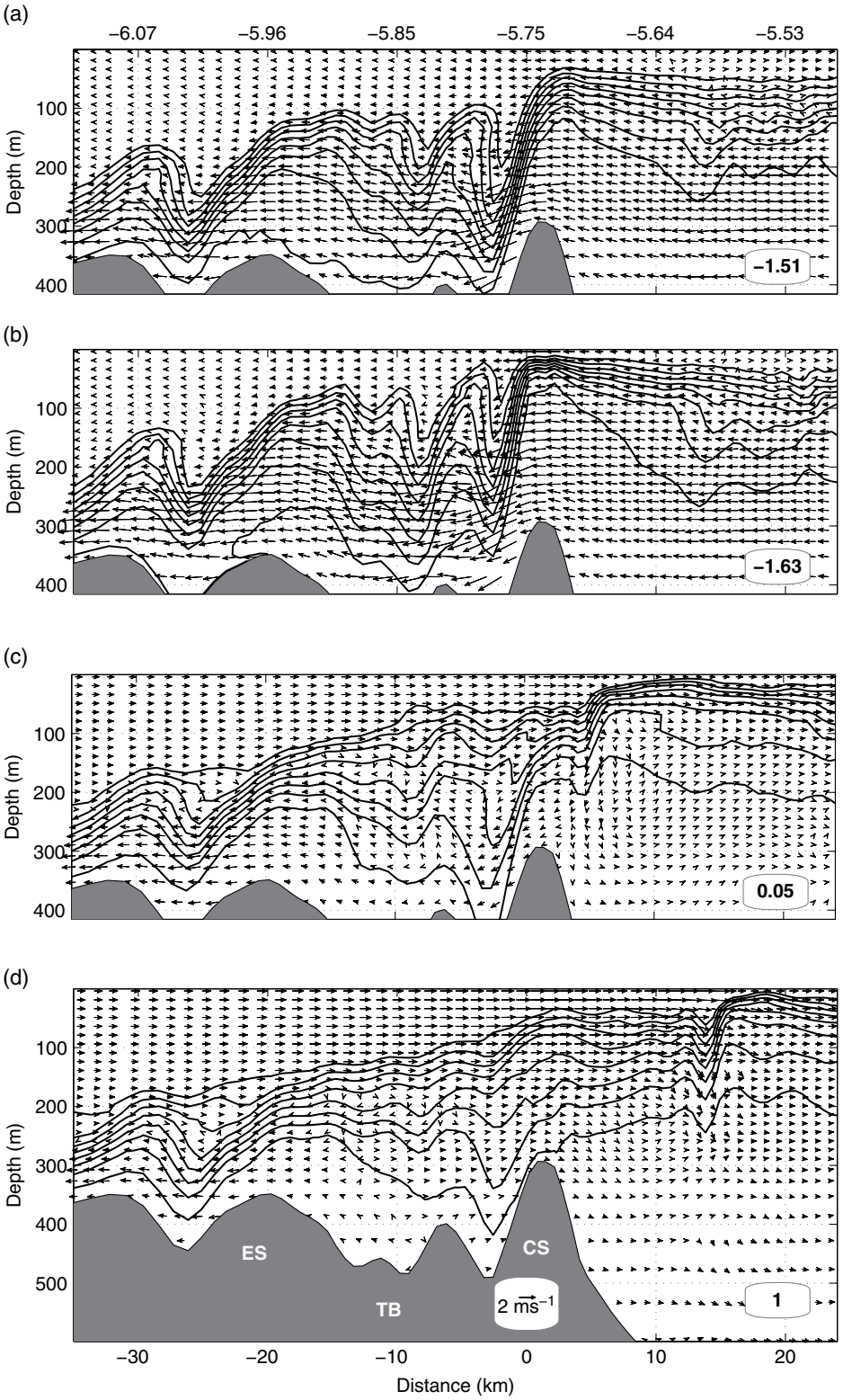

Figure 3.15 Same as Figure 3.14, but with an increased number of iterations (5) for the Smolarkiewicz advection scheme (EXP2).

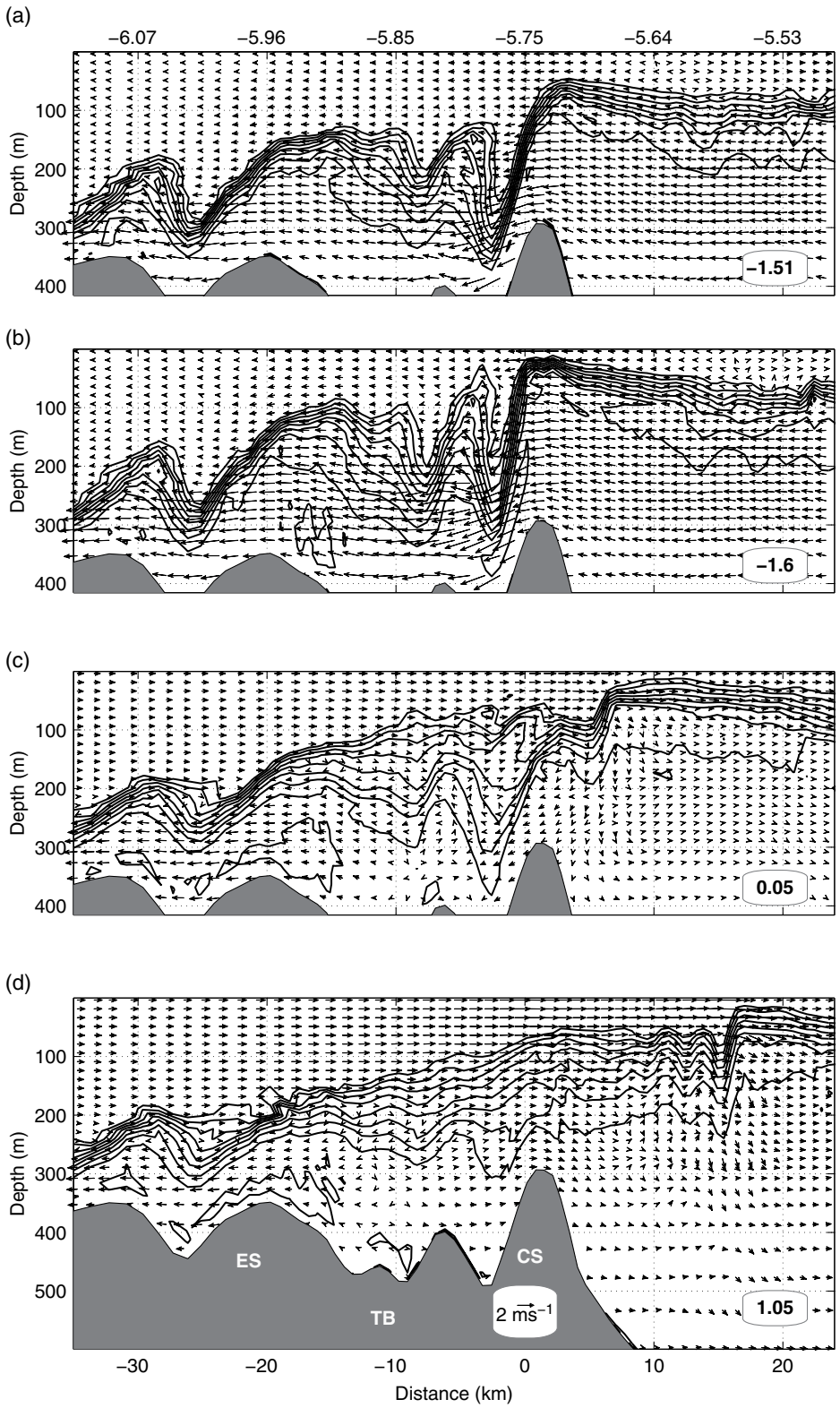

Figure 3.16 Same as Figure 3.15, but with the horizontal diffusivity set to zero (EXP3).

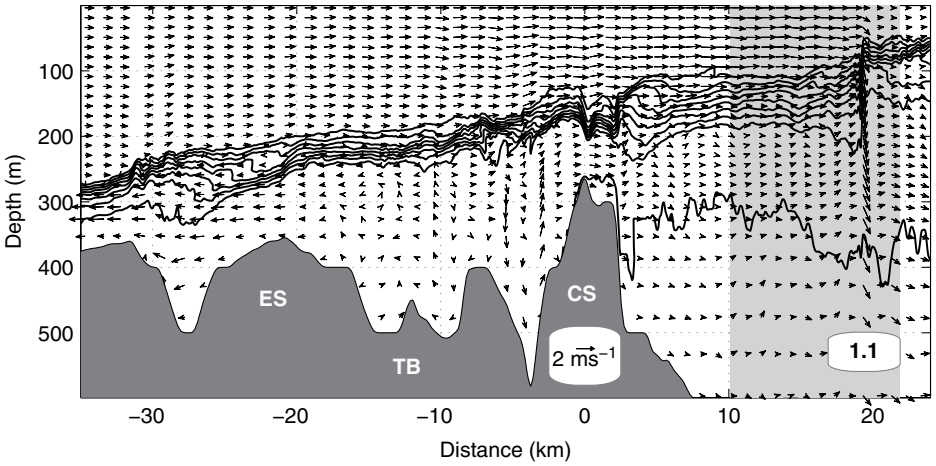

Figure 3.17 Same as Figure 3.4, but with the nonhydrostatic feature off.

3.5. DISCUSSION AND CONCLUSION

The flow exchange through the SoG simulated by a high-resolution σ-coordinate hydrostatic model has been compared with that simulated by a very high-resolution, z-coordinate, nonhydrostatic model. The hydrostatic model used is POM as implemented by *Sannino et al*. [2009a]. Differently from the original version of POM (generally known as *pom*98), the model implemented for the SoG used the MPDATA advection scheme as implemented by *Sannino et al*. [2002]. MPDATA has been subsequently included in the official version of POM (known as *pom*2*k*).

We stress that the implementation of MPDATA was absolutely necessary because of the presence of strong density contrasts associated with intense tidal currents present in the SoG that made the dispersive second-order–centered advection scheme (the only advection scheme present in *pom*98), unable to reproduce the water exchange. The POM implementation has been positively validated by different authors against most of the *in situ* data. However, due to the scarcity in space of long and high frequency temporal measurements, an overall analysis of the model results was still necessary.

A common method to assess the validity of a numerical simulation consists in comparing the model results against a sort of numerical "true" solution, that is, a solution obtained by a very high-resolution numerical model characterized by more robust physical parameterizations. Thus, in this paper we have compared the hydrostatic model results with those obtained by a very high-resolution z-coordinate nonhydrostatic model. The nonhydrostatic model used is the MITgcm implemented for the SoG at a horizontal resolution of about 50 m on the middle of the strait. MITgcm was initialized and laterally forced as a one-way nested model of the POM simulation.

The two models differ primarily in their horizontal resolution. POM has a maximum resolution in the strait of about 300 m, while MITgcm reaches in the same region of the strait about 50 m. In other words, MITgcm adopts a resolution six times finer than POM. A less-marked difference is in the vertical discretization. POM has 32 σ-levels, and MITgcm 53 z-levels. In the middle of the strait, in a water depth of 500 m, POM has a resolution of about 8 m in the upper and lower 50 m, and a resolution of 20 m for the remaining 400 m. MITgcm uses 53 z-levels spaced 7.5 m in the upper 300 m and with spacing that gradually increases to a maximum of 105 m for the remaining 13 bottom levels.

As expected, nonhydrostatic effects have an impact on the simulated internal wave field. In the hydrostatic POM model, the internal bore does not undergo its classical evolution into a series of short easterly propagating solitary waves as predicted by weakly nonlinear theories. The MITgcm nonhydrostatic simulation does simulate this process in a way that is qualitatively faithful. Differences also have been found in the way the two models reproduce the three-layer hydraulic regime and transports. MITgcm displays a more marked along-strait variability of supercritical flow regions due to the finer description of the bathymetry (Figure 3.11). However, looking at the frequency of occurrence of supercritical flow with respect to both modes, not only in single sections but in larger areas around the three main hydraulic regions, it can be seen that the MITgcm predicts a similar supercritical flow along TN (gray bars in Figure 3.13).

On the contrary, looking at the frequency of occurrence of supercritical flow with respect to one mode, it can be seen that the maximum difference between the two model simulations is confined to TN. Here MITgcm predicts a frequency 28% less than POM (from 70% to 42%), while a minor reduction affected ES (from 74% to 62%), and

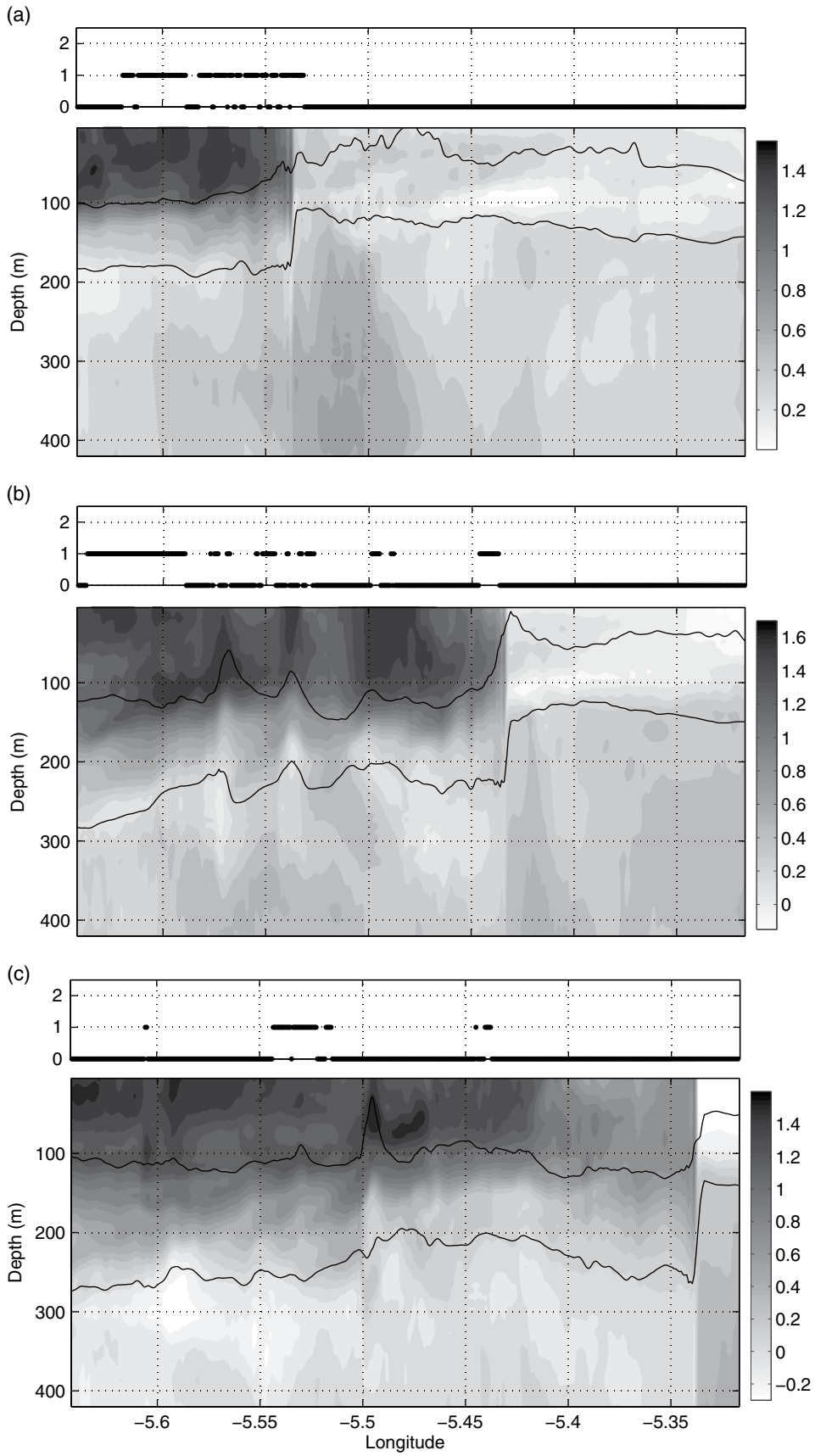

Figure 3.18 Same as left panels in Figure 3.12, but with the nonhydrostatic feature not considered.

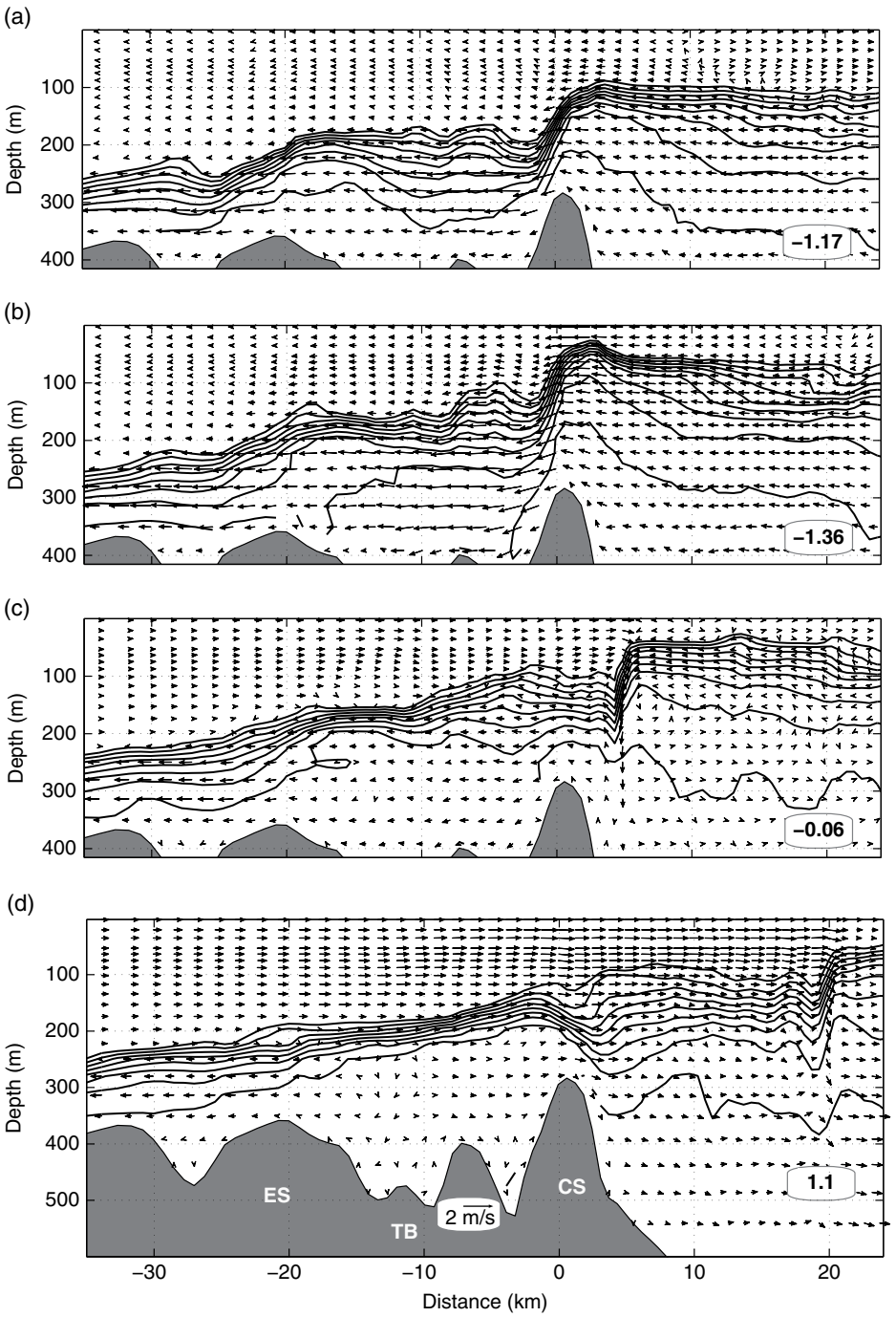

Figure 3.19 Time-evolution of isohalines 36.40, 36.65,…,38.65 and velocity currents simulated by MITgcm using the model grid initially used for POM (EXP5) during one tidal cycle of moderate tidal strength. The barotropic velocity (in ms^{-1}) over Camarinal Sill is indicated at the lower right corner of the panels. Elapse times after panel a are 1:40 h (panel b), 4:40 h (panel c), and 7:00 h (panel d).

almost similar values were obtained for CS (from 41% to 48%). The larger difference is due to the systematic underestimation of the upper layer along TN produced by POM (Figure 3.6). This is particularly clear comparing the evolution of a propagating bore across a section in TN together with the associated hydraulic regime of the flow as simulated by MITgcm and POM, respectively (Figure 3.12). It is shown that, in contrast to POM, MITgcm achieves the control only when the eastward bore is present in TN. The different hydraulic behavior is

the result of a different representation of the three-layer thickness (Figure 3.7). While the three-layer thickness simulated by MITgcm is in good agreement with that derived from observed salinity profiles (Figure 6 in *Bray et al*. [1995]), POM overestimates the interface layer thickness and consequently underestimates both the upper and lower layers' thickness. The overestimation is attributed to the excess of spurious diapycnal mixing produced by POM that overshadows the naturally occurring mixing. The large spreading of the isohalines along the SoG present in the POM simulation (Figure 3.3), in comparison with those obtained by MITgcm (Figure 3.4), clearly shows that the simulated internal wave propagation induces a greater level of spurious diapycnal diffusion in POM.

To investigate the origin of such spurious diapycnal mixing, three additional experiments were performed to examine the sensitivity of the POM results to the choice of the coefficients governing the tracers diffusivity parameterization (EXP1-3). From these experiments, the numerically induced mixing was found to be due to the adopted advection scheme (MPDATA).

An additional experiment was carried out to explore the impact of the nonhydrostaticity on the simulated hydraulic regime. MITgcm was rerun in hydrostatic mode (EXP4). Results indicated that the hydraulic regime was not affected by the hydrostatic limitation.

A further experiment was performed to examine the influence of the horizontal and vertical resolution on the simulated exchange flow (EXP5). MITgcm was implemented on the same horizontal grid as for Exp-POM, and with a z-level distribution that ensured a vertical resolution similar to Exp-POM. Results indicated that the hydraulic regime remained very similar to that of EXP4 and, consequently, to Exp-MIT.

To conclude, the results of the experiments can be used to derive some general rules to correctly model the exchange flow through the SoG. First, the horizontal resolution similar to the one adopted in Exp-POM is enough for simulating the hydraulic regime of the SoG. Second, the nonhydrostatic formulation is not strictly necessary for simulating the hydraulic regime. Finally, the application of diffusive advection schemes, such as MPDATA in high-resolution σ-coordinate models used to simulate a tidally forced large internal wave, can potentially be a source of spurious diapycnal mixing. As a general recommendation in these cases, we suggest maintaining horizontal diffusion as small as possible in order to alleviate, at least in part, the spurious mixing.

Acknowledgments. We are grateful to the CRESCO supercomputing facilities located at ENEA (http://www.cresco.enea.it). Pratt is supported by National Science Foundation Grant OCE-0927017. The authors would also like to thank the anonymous referees whose comments helped improve this manuscript.

REFERENCES

Adcroft A., and J. M. Campin (2004), Rescaled height coordinates for accurate representation of free-surface flows in ocean circulation models, *Ocean Modelling*, *7*, 34, 269–284.

Armi, L., and D. M. Farmer (1988), The flow of Atlantic water through the Strait of Gibraltar, *Progress in Oceanography 21*, 1–105.

Bills, P., and J. Noye (1987), *Numerical Modelling: Applications to Marine Systems*, Elsevier Science Publishers.

Blumberg, A. F., and G. L. Mellor (1987), *A description of a three-dimensional coastal ocean circulation model*, n. s. heaps Edition, American Geophysical Union, Washington D.C.

Bray, N., J. Ochoa, and T. H. Kinder (1995), The role of the interface in exchange through the Strait of Gibraltar, *J. Geophys. Res.*, *100*, 10755–10776.

Bryden, H., and H. Stommel (1984), Limiting processes that determine basic features of the circulation in the Mediterranean Sea, *Oceanologica Acta*, *7* (3), 289–296.

Campin, J. M., A. Adcroft, C. Hill, and J. Marshall (2004), Conservation of properties in a free-surface model, *Ocean Modelling*, *6*, 34, 221–244.

Candela, J., C. Winant, and A. Ruiz (1990), Tides in the Strait of Gibraltar, *J. Geophys. Res.*, *95*, 7313–7335.

Carter, G. S., and M. A. Merrifield (2007), Open boundary conditions for regional tidal simulations, *Ocean Modelling*, *18* (3–4), 194–209.

Egbert, G. D., and L. Erofeeva (2002), Otis-osu tidal inversion software, www.coas.oregonstate.edu/research/po/research/tide/otis.html.

Ezer, T. (2005), Entrainment, diapycnal mixing and transport in three-dimensional bottom gravity current simulations using the Mellor-Yamada turbulence scheme, *Ocean Modelling*, *9*, 151–168.

Farmer, D. M., and L. Armi (1988), The flow of Mediterranean water through the Strait of Gibraltar, *Prog. Oceanogr.*, *21*, 1–105.

Fringer, O., M. Gerritsen, and R. Street (2006), An unstructured-grid, finite-volume, nonhydrostatic, parallel coastal ocean simulator, *Ocean Modelling*, *14*, 139–278.

Garrido, J. C. S., G. Sannino, L. Liberti, and L. Pratt (2012), Numerical modeling of three-dimensional stratified tidal flow over Camarinal Sill, Strait of Gibraltar, jgr 116 (C12026), doi:10.1029/2011JC007093.

Garrido, J. C. S., J. G. Lafuente, F. C. Aldeanueva, A. Baquerizo, and G. Sannino (2008), Time-spatial variability observed in velocity of propagation of the internal bore in the Strait of Gibraltar, jgr 113 (C7).

Griffies, S., R. Pacanowski, and R. Hallberg (2000), Spurious diapycnal mixing associated with advection in a z-coordinate ocean model, *Mon. Wea. Rev.*, *128* (3), 538564.

Haney, R. L. (1991), On the pressure gradient force over steep topography in sigma coordinate ocean models, *J. Phys. Oceanogr.*, *21*, 610–619.

Hundsdorfer, W., B. Koren, M. Vanloon, and J. Verwer (1995), A positive finite-difference advection scheme, *J. Computational Physics*, *117* (1), 35–46.

Lacombe, H., and C. Richez (1982), *Hydrodynamics of Semi-Enclosed Seas*, Elsevier, Amsterdam.

Legg, S., R. Hallberg, and J. Girton (2006), Comparison of entrainment in overflows simulated by z-coordinate, isopycnal and non-hydrostatic models, *Ocean Modeling*, *11* (1–2), 69–97.

Leith, C. (1968), Parameterization of vertical mixing in numerical-models of tropical oceans, *Physics of Fluids*, *10*, 1409–1416.

Marchesiello, P., L. Debreu, and X. Couvelard (2009), Spurious diapycnal mixing in terrain-following coordinate models: The problem and a solution, *Ocean Modelling*, *26* (3–4), 156–169.

Marshall, J., A. Adcroft, C. Hill, L. Perelman, and C. Heisey (1997a), A finite-volume, incompressible Navier Stokes model for, studies of the ocean on parallel computers, *J. Geophys. Res.*, *102* (C3), 5753–5766.

Marshall, J., C. Hill, L. Perelman, and A. Adcroft (1997b), Hydrostatic, quasi-hydrostatic, and nonhydrostatic ocean modeling, *J. Geophys. Res.*, *102* (C3), 5733–5752.

MEDAR Group (2002), Medatlas/2002 database, Mediterranean and Black Sea database of temperature salinity and bio-chemical parameters, *Climatological Atlas*, IFREMER Edition.

Mellor, G., and T. Yamada (1982), Development of a turbulence closure model for geophysical fluid problems, *Reviews of Geophysics and Space Physics*, *20* (4), 851–875.

Mellor, G., T. Ezer, and L. Oey (1994), The pressure gradient conundrum of sigma coordinate ocean models, *J. of Atmospheric and Oceanic Technology*, *11* (4 part 2), 1126–1134.

NOAA (2001), (ETOPO2) 2-minute gridded global relief data.

Orlanski, I. (1976), A simple boundary condition for unbounded hyperbolic flows, *J. Computational Physics*, *21*, 251–269.

Pacanowski, R., and S. Philander (1981), Parameterization of vertical mixing in numerical-models of tropical oceans, *J. Phys. Oceanogr.*, *11* (11), 1443–1451.

Pickart, R. S., L. J. Pratt, D. J. Torres, T. E. Whitledge, A.Y. Proshutinsky, K. Aagaard, T. A. Agnew, G. W. K. Moore, and H. J. Dail (2010), Evolution and dynamics of the flow through Herald Canyon in the western Chukchi Sea, *Deep-Sea Research II*, *57*, 5–26.

Pratt, L. (2008), Critical conditions and composite Froude numbers for layered flow with transverse variations in velocity, *J. Fluid Mech.*, *602*, 241–266.

Sanchez-Roman, A., G. Sannino, J. Garcia-Lafuente, A. Carillo, and F. Criado-Aldeanueva (2009), Transport estimates at the western section of the Strait of Gibraltar: A combined experimental and numerical modeling study, *J. Geophys. Res.*, 114.

Sannino, G., A. Bargagli, and V. Artale (2002), Numerical modeling of the mean exchange through the Strait of Gibraltar, *J. Geophys. Res.*, *107* (8), 9 1–24.

Sannino, G., A. Bargagli, and V. Artale (2004), Numerical modeling of the semidiurnal tidal exchange through the Strait of Gibraltar, *J. Geophys. Res.*, *109*, C05011, doi:10.1029/2003JC002057.

Sannino, G., A. Carillo, and V. Artale (2007), Three-layer view of transports and hydraulics in the Strait of Gibraltar: A three-dimensional model study, *J. Geophys. Res.*, *112*, C03010, doi:10.1029/2006JC003717.

Sannino, G., L. Pratt, and A. Carillo (2009a), Hydraulic criticality of the exchange flow through the Strait of Gibraltar, *J. Phys. Oceanogr.*, *39* (11), 2779–2799.

Sannino, G., M. Herrmann, A. Carillo, V. Rupolo, V. Ruggiero, V. Artale, and P. Heimbach (2009b), An eddy-permitting model of the Mediterranean Sea with a two-way grid refinement at the Strait of Gibraltar, *Ocean Modelling*, *30*, 1 56–72.

Sanz, J., J. Acosta, M. Esteras, P. Herranz, C. Palomo, and N. Sandoval (1992), Prospeccin geofsica del estrecho de Gibraltar (resultados del programa hrcules 1980–1983), *Publ. Espec. Inst. Esp. Oceanogr.*, *7*, 48.

Smagorinsky, J. (1963), General circulation experiments with primitive equations, i: The basic experiment, *Mon. Wea. Rev.*, *91*, 99–164.

Smolarkiewicz, P. (1984), A fully multidimensional positive definite advection transport algorithm with small implicit diffusion, *J. Comput. Phys.*, *54*, 325–362.

Vlasenko, V., J. C. Sanchez Garrido, N. Stashchuk, J. Garcia Lafuente, and M. Losada (2009), Three-dimensional evolution of large-amplitude internal waves in the Strait of Gibraltar, *J. Phys. Oceanogr.*, *39*, (9), 2230–2246.

Wesson, J., and M. Gregg (1994), Mixing at Camarinal Sill in the Strait of Gibraltar, *J. Geophys. Res.*, *99* (C5), 9847–9878.